Vol. 473: 29–51, 2013
doi: 10.3354/meps10049

MARINE ECOLOGY PROGRESS SERIES
Mar Ecol Prog Ser

Published January 21

Characterization of biophysical interactions in the water column using *in situ* digital holography

Siddharth Talapatra[1], Jiarong Hong[1], Malcolm McFarland[3], Aditya R. Nayak[1], Cao Zhang[1], Joseph Katz[1,*], James Sullivan[2], Michael Twardowski[2], Jan Rines[3], Percy Donaghay[3]

[1]The Johns Hopkins University, Baltimore, Maryland 21218, USA
[2]WET labs Inc., Narragansett, Rhode Island 02882-1197, USA
[3]University of Rhode Island, Graduate School of Oceanography, Narragansett, Rhode Island 02882-1197, USA

ABSTRACT: A free-drifting submersible holography system, 'Holosub', was deployed in East Sound, Washington as part of a collaborative field study. Analysis of more than 20 000 holograms recorded during 2 slow profiling ascents (that avoided disturbance to the parameters measured) provided the size and spatial distributions of particles, the orientation of diatom chains, and the mean shear strain and turbulence dissipation rate profiles. This information was complemented by concurrently measured parameters including density, chlorophyll *a* concentration and optical scattering, and discrete water sampling for species characterization. Key findings were: (1) a prominent thin layer of mostly non-motile small particles, many of them chlorophyll *a* rich, formed in a region of near-zero shear and low dissipation rates, and high stratification; (2) multiple particle concentration peaks formed at several depths with low shear and dissipation rates; (3) *Chaetoceros socialis* colonies had several volume fraction peaks near the pycnocline, with the largest coinciding with the thin layer and some smaller peaks coinciding with small particle peaks; (4) zooplankton avoided many regions with elevated *C. socialis* and/or particle concentrations; (5) diatom chains had nearly horizontal alignment (zero angle) in the thin layer, with low angles also observed in other low shear/dissipation regions, and random orientations in several local shear/dissipation maxima regions; and (6) comparisons between particle counts from on-board cell cytometry, microscopic digital holography, and light microscopy of discrete samples showed similarities in trends but also discrepancies. In addition to these specific findings, this study demonstrates the great potential of digital holography for *in situ* studies of biophysical interactions and particle dynamics in oceanic flows.

KEY WORDS: Holography · Submersible · Shear · Dissipation · Biophysical interactions

INTRODUCTION

The spatial distribution of plankton in the oceanic water column has a direct bearing on biological and physical processes in the marine ecosystem (Cowles et al. 1998, Sullivan et al. 2010a). Understanding *in situ* plankton behavior, such as predator-prey interaction, species concentration and interaction of organisms with the surrounding flow can lead to better models to predict occurrences of events such as harmful algal blooms (Donaghay & Osborn 1997, McManus et al. 2008). Early studies of the patchiness in physical and biochemical patterns focused on large scales, typically tens of meters or larger (e.g. Cassie 1963, Haury et al. 1978). It has been recognized that fine-scale patchiness is critical to the interaction between physicochemical parameters and biology (Valiela 1995, Ryan et al. 2010). A particular phenomenon that has received substantial attention is formation of vertically layered, thin patches of

*Corresponding author. Email: katz@jhu.edu

marine plankton, termed 'thin layers' (Derenbach et al. 1979), often found in regions of physical discontinuities such as pycnoclines (McManus et al. 2005). Studies, e.g. those by Dekshenieks et al. (2001), Sullivan et al. (2010b) and Durham & Stocker (2012), have shown that these thin layers have vertical depths typically varying from a few centimeters to a few meters, while their horizontal extent can be in kilometers and their temporal extent can vary from an hour to several weeks.

Heterogeneities in the distribution of plankton in the water column, especially thin layers, can have a significant influence on ecosystem ecology by controlling patterns of primary productivity, trophic transfer, fish larvae survival, etc. There are numerous studies focused on understanding the formation of heterogeneities in the water column, and mechanisms responsible for their stability/instability. A common approach is to postulate the formation of thin layers in regions where 'convergent' forces that thin a phytoplankton layer exceed the 'divergent' forces that broaden the layer (Osborn 1998, Stacey et al. 2007). Convergent forces that contribute to formation and maintenance mechanisms include straining by shear (Birch et al. 2008), buoyancy-driven settling of particles along a pycnocline (Franks, 1992) and active swimming by phytoplankton (Durham et al. 2009, Sullivan et al. 2010b). In addition to physical factors, phytoplankton can accumulate in layers in response to the availability of nutrients, presence of predators or for reproduction (Leising 2001). The primary divergent process is turbulent diffusion (Wang & Goodman 2010) caused by a variety of physical processes such as winds, non-linear internal waves and convective overturns. Field studies on the interplay of these biophysical factors have been presented by e.g. Alldredge et al. (2002), who performed simultaneous measurements of abundances of marine snow aggregates, phytoplankton and zooplankton along with various physical parameters. This study not only showed broad correlation between the presence of thin layers of marine snow or phytoplankton and pycnoclines, but also provided evidence for the preferential aggregation of zooplankton with respect to marine snow.

Numerous *in situ* instruments and deployment techniques have been developed to sample the water column at fine scales. For example, 'slow-drop' vertical profiling, where the sampling platform is both decoupled from ship motion and ballasted to be slightly negatively buoyant, can achieve vertical sampling resolution at centimeter scales (e.g. Donaghay et al. 1992, Cowles et al. 1998). Multi-frequency acoustic profiling sensors have been developed to locate large concentrations of zooplankton at fine scales (Holliday et al. 1998, Benoit-Bird et al. 2010), and spatial variability of the volume scattering function (VSF) has been used to identify high concentrations of particulates and organisms (Twardowski et al. 1999, Sullivan et al. 2005, 2010b). Acoustic Doppler Current Profilers (ADCPs) have been commonly used to measure mean shear rates in the water column (e.g. McManus et al. 2005), but ADCPs have a highest depth resolution of ~1 m, which could be insufficient to study how the flow physics affects the formation of particle layers.

The present study is motivated by the fact that a more complete understanding of population dynamics, plankton behavior and species composition requires identification and quantification of the 3-dimensional (3D) spatial distribution of various particles and organisms throughout the water column, in a non-intrusive manner. Underwater video imaging (Davis et al. 1992) has been used to make direct observations of marine life and their abundances with depth, but it lacks the ability to maintain focus over a significant thickness, thus providing information only in a small volume of fluid. The current work utilizes free stream holography, which has the ability to maintain high lateral resolution in a sample volume with substantial thickness. This advantage enables tracking of organisms and the determination of the 3D spatial distribution of different organisms and particles at high resolution, and in an undisturbed volume. Thus, a submersible with an on-board holographic optical setup would serve as an ideal tool to study the water column. Several submersible holography systems have been developed, starting with the holographic velocimeter which measured size and settling rates of particulate matter (Carder 1979). Pulsed laser based submersible holographic systems, which recorded holograms on high resolution film, have since been developed by Katz et al. (1984), O'Hern et al. (1988), Katz et al. (1999), Malkiel et al. (1999, 2004) and Watson et al. (2001). Though use of film enabled these researchers to study large sample volumes without compromising resolution, these systems involved cumbersome instrumentation, and long processing and data analysis times. However, the results in Katz et al. (1984), and Malkiel et al. (2004) resolved relationships among spatial distributions of multiple species that could not have been studied by any other means. While switching to digital holography involves a compromise in resolution, the advantages in live transmission of holograms and a much larger data acquisition capacity outweigh its

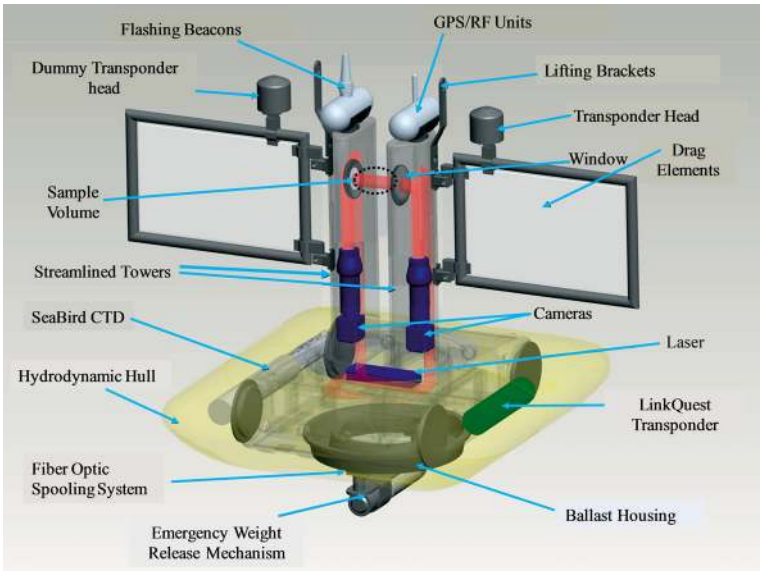

Fig. 1. Schematic of the Holosub used to study biophysical interactions in the water column at East Sound, Washington, USA. Red: laser beam

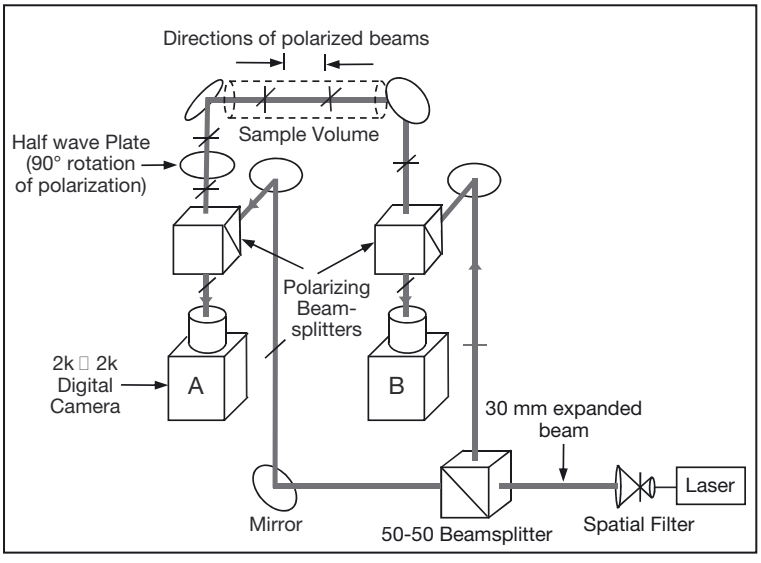

Fig. 2. Optical line-up for the dual camera digital in-line holographic setup

disadvantage. Furthermore, the emergence of compact diode-pumped solid-state lasers has reduced the size of the optical setup to a small fraction of the original systems. The first *in situ* implementation of digital holography was by Owen & Zozulya (2000), who used a low power continuous diode laser and a charge-coupled device camera, followed by Jericho et al. (2006) who recorded organisms trapped in an isolation chamber, the pulsed laser based system built by Sun et al. (2007) for measuring size distributions of copepods, and the sediment measurement system developed by Graham & Smith (2010). In all of these cases, the results were based on analyzing a small number of particles/organisms. This paper focuses on data obtained during a recent deployment in East Sound, Washington, USA of the Holosub — a free drifting, submersible, ballast-controlled, multi-camera, digital holography system (Pfitsch et al. 2005, 2007). We start with a brief description of the instrumentation and the deployment details, followed by an explanation of key data analysis steps. Results are presented and analyzed with the goal of elucidating some of the underlying mechanisms responsible for heterogeneities in the distributions of particles and organisms in the water column.

MATERIALS AND METHODS

The Holosub

A detailed description of the instrumentation associated with the Holosub has been provided by Pfitsch et al. (2005), and is summarized briefly here. An illustration of this system, as deployed, is provided in Fig. 1, and its internal optical setup is sketched in Fig. 2. A 10 cm long cylinder-shaped sample volume is located between the 2 streamlined vertical towers, whose shape and height (55 cm, with the sample volume located 12 cm below the top) are designed to minimize the flow disturbance in the imaged sample volume. Drag-inducing elements are attached to the towers, at the same elevation as the transparent viewing windows, in order to reduce the relative motion between the platform and the local currents while the submersible is drifting. Streamlined shells cover the main body of the submersible, to minimize the drag of the parts of the device that are relatively far from the windows. In the 'profiling mode' (not discussed here), the drag elements and streamlined shells are removed, as the submersible is rapidly lowered and raised through the water column. A communication line connecting the submersible to a host computer located on a boat consists of a single mode fiber optic cable, which

transmits data in 4 channels, each at a different wavelength. One of these channels is used for controlling the 2 cameras, laser, ballast pump, etc. The other 3 channels are used for transmitting the CTD output and the digital holograms from the 2 cameras. All electrical signals are converted into optical signals prior to transmission and then converted back, either on the surface for storage, display and analysis, or inside the Holosub for implementation of user commands. The optical fiber can either be released from the boat, as was done during these experiments, or released from a spool located on the platform. The latter reduces the drag on the Holosub by increasing the slack of the fiber optic cable. We did not utilize this option during this study, owing to convenience and the low current velocities encountered during the deployments. The submersible is powered by Lithium ion batteries, which typically support 1.5 h of operation. The Holosub has an onboard ballast control mechanism, consisting of a positive displacement pump, associated drivers and a rubber tube, which is located inside a sealed air chamber under the platform. Pumping of seawater in and out of the tube modifies its buoyancy, thereby controlling its depth and descent/ascent rates. The CTD data are used for monitoring the system depth in real time, thereby allowing the operator to remotely control its vertical motion. The density data acquired by this CTD were unusable since the sample water was not pumped from the vicinity of the sample volume. This shortcoming will be rectified in future deployments. However, the depth was recorded accurately, as verified by comparing its data to measurements performed by an acoustic doppler velocimeter (ADV) that was attached to the platform during some of the deployments. As discussed in the next sub-section, profiles of density and optical scattering from particles were measured by other simultaneously deployed instruments.

The optical setup used during the present deployments (Fig. 2) consists of 2 in-line holography systems with different magnifications that propagate in opposite directions. In-line holography involves illumination of the sample volume with a collimated laser beam, and recording the interference pattern of light scattered by the particles in the sample volume, with the undisturbed part of the beam. The recorded holograms are transferred to a computer where they are numerically reconstructed using the Fresnel-Kirchoff formula (Katz & Sheng 2010), plane by plane, to obtain a series of in-focus images of particles in the sample volume. In the present configuration, light from a pulsed (50 ns duration), diode-pumped, 660 nm neodymium-doped yttrium lithium fluoride (Nd:YLF) laser is split into 2 beams, which cross the same sample volume from opposite directions. Polarizing beam splitters and half wave plates ensure that these overlapping beams have orthogonal polarizations in order to avoid interference. The holograms are recorded at 14.7 frames s^{-1} by a pair of 2048 × 2048 pixel digital cameras, i.e. the data acquisition rate is 117.6 MB s^{-1}. Camera A records holograms at a resolution of 3.9 µm $pixel^{-1}$ with a field of view of 8 × 8 mm, which is embedded within the 11.5 × 11.5 mm field of view of camera B, which records holograms at a resolution of 5.7 µm $pixel^{-1}$. In all, 6 TB, i.e. 1.5 million holograms, were recorded over the 2 wk deployment, covering 7.4 h of net profiling time at different locations, times and flow conditions.

Other instrumentation and deployment details

The Holosub was deployed during May 2010 in EastSound — a fjord on Orcas Island, Washington — as part of a collaborative field experiment with researchers from WET labs, the University of Rhode Island (URI), National Oceanic and Atmospheric Administration (NOAA) and Naval Research Lab. Three surface vessels and numerous instruments were deployed simultaneously, only a few of which are discussed in this paper. An aircraft operated by NOAA collected daily light detection and ranging (LIDAR) data (Churnside & Donaghay 2009) nearly synoptically over all of East Sound, providing locations of thin layers in real time, and relaying their positions to surface boats. Researchers from WET labs deployed a vertical profiler simultaneously with the Holosub, from the same boat. This profiler was equipped with a SeaBird SBE-49 CTD, a WET labs ac-s, an ECO-BB3, a LISST-100 and the Multi-Angle Scattering Optical Tool (MASCOT) VSF device (Twardowski et al. 1999). The ac-s is a hyper-spectral (>80 wavelengths) light absorption and attenuation meter. The ECO-BB3 is a 3 wavelength backscattering sensor (470, 532, 650 nm) at one angle (124°). The LISST-100 is a laser diffractometer that measures the near-forward VSF and particle size distribution (PSD) based on Mie theory inversion, and the MASCOT measures the *in-situ* VSF of monochromatic light (658 nm) from 10° to 170°, at 10° intervals.

On the URI research vessel, data from the high-resolution profiler were used to identify depths for subsequent collection of discrete water samples, using a Ruttner design sampler (KC Denmark). Each sample was split into multiple aliquots, and analyzed, on

board the URI vessel, as follows: (1) ~750 ml was gently sieved (20 µm pore), and examined live on a Zeiss microscope with phase contrast optics. A checklist of the phytoplankton species present was compiled, qualitative observations were made on the morphology and life history of individual taxa and a color video record was made of each slide. This information was used to aid in the identification of phytoplankton imaged by the cinematic, in-line microscopic holography system. (2) A CytoSense scanning flow cytometer was used to count individual particles (unicellular organisms and colonies) and characterize their size, shape, pigment content and scattering. Both the original and the concentrated samples described above were characterized with the flow cytometer. (3) A cinematic in-line microscopic holography system was used to record holograms in a sample volume of 1.75 × 1.75 × 10 mm^3 located within a 1 × 1 × 5 cm^3 lucite cuvette, at a resolution of 1.71 µm $pixel^{-1}$, and an acquisition rate of 250 Hz. In conjunction with the on-board light microscopy of living material, these images assisted in identification of the predominant taxa present in Holosub images. This device facilitated observations of the swimming behavior of different organisms. The on-board holography system also enabled counting of particles with a minimum size of 4 µm. (4) 125 ml of whole water was preserved in 1% formaldehyde and 1% glacial acetic acid and returned to Rhode Island, where individual cells in selected samples were quantified. Phytoplankton cells >8 µm were counted in a Sedgewick Rafter chamber on a Nikon Eclipse E800 microscope using a 10× objective.

The results presented in this paper are based on analysis of data acquired in the afternoon of May 14, while the Holosub was drifting, during 2 slow (2 cm s^{-1} average) ascents, separated by 40 min, hereafter referred to as Ascents I and II, whose time-histories are shown in Fig. 3. We only utilized data recorded while the vehicle was climbing slowly through the water column in order to minimize the hydrodynamic impact of the platform on the flow/fluid within the sample volume. A total of 19 200 and 21 260 holograms were recorded by both cameras during Ascents I and II, respectively, along with their corresponding depths. Only a subset of these data was analyzed, as explained below.

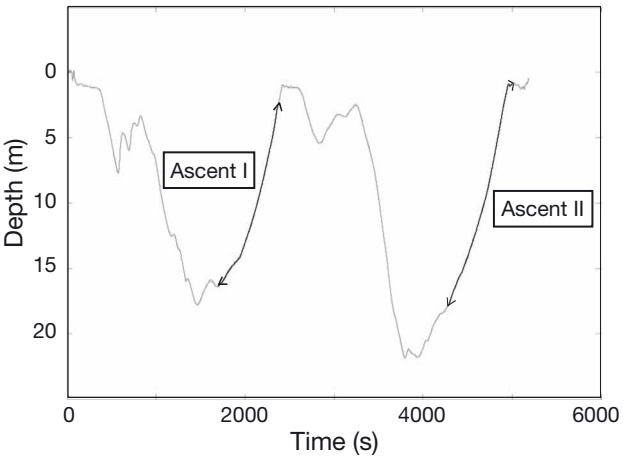

Fig. 3. Temporal depth variation of the Holosub obtained from the CTD data, during a run (Ascents I and II) on 14 May 2010

Data analysis procedures

To identify particles to the best of our ability, we used the higher resolution, 3.9 µm $pixel^{-1}$ holograms, with 8 × 8 mm field of view. There were 9600 and 10 630 higher resolution holograms recorded during Ascents I and II, respectively. For quantitative analysis, particles were divided into 4 broad categories: (1) 'small particles' in the 10–200 µm size range, where the classification 'small' is purely based on the Holosub resolution, (2) the typically large, spherical colonies of the diatom *Chaetoceros socialis*, (3) straight or helical diatom chains, and (4) zooplankton, including copepods and nauplii. It must be noted that for calculating the concentration profiles of small particles, diatom chains and zooplankton, the volumes in front and behind the large *C. socialis* colonies, where individual particles might be obscured, were excluded from the sample volume. In order to prevent counting the same particle more than once and reduce computation costs, 1 in 5 holograms were used for analysis of particle distributions, which gave an average sampling rate of 1 hologram per 6.55 mm traversed by the Holosub. As a result, a total of 1920 and 2126 holograms were analyzed for Ascents I and II, respectively, in this analysis. The following steps were utilized to quantify the *in situ* distributions of the different particle categories, the *in situ* shear strain and dissipation rates, and the cell concentrations in the collected samples:

Calculating in-focus images

In-focus images of particles >100 µm were generated by reconstructing each hologram over the entire 10 cm sample volume thickness, in steps of 1 mm, dividing the 2048 × 2048 pixel reconstructed planes into 128 × 128 pixel windows, and then choosing the

location that brought the largest object in each window into focus. For most windows, a simple method to detect the location of in-focus images was to select the plane with the maximum number of pixels with intensities below a specified threshold. Subsequently, edge detection was also performed selectively when minimization of intensity failed. This hybrid method brought most of the large particles into focus, providing a quick and effective way to qualitatively analyze the large sample volume. Diatom chains, both linear and helical, as well as zooplankton consisting of copepods and nauplii, were identified visually from these in-focus images.

Small (10–200 µm) particle statistics

These were extracted by reconstructing each hologram in steps of 0.1 mm. The images were then box band-pass filtered, with a 3 × 3 pixel low-pass filtering used to reduce the laser speckle noise, and a 40 × 40 pixel high-pass filtering was used to remove the large particles from the images. The images were then collapsed onto a single plane by selecting the lowest intensity for each pixel. Image segmentation was subsequently performed to define the boundaries of each particle, measure their size and aspect ratio, and discard the elongated diatom chains. Particles with mean diameters <10 µm were also discarded, since distinguishing real particles from noise was unreliable below this scale at this magnification.

Chaetoceros socialis colony statistics

To extract statistics for *Chaetoceros socialis* colonies, the holograms were reconstructed, in steps of 2 mm, and then low-pass filtered using 5 × 5 pixel box filters to remove small particles. After image segmentation, followed by filtering based on aspect ratio and size, the cross-sectional areas of the colonies were recorded, which appeared as 'blobs' in the intensity-combined images. The mean diameter of each colony, computed from the area, was used to estimate its volume, using a simplifying assumption of spherical colonies. Adding all such volumes in a specific hologram, and dividing it by the sample volume (6.4 ml) provided an estimate for the *C. socialis* volume fraction. The Holosub data, along with the high resolution holograms recorded by the on-board holographic microscope, were also utilized to estimate the average number of cells in a *C. socialis* colony. Then, based on the concentration of colonies in situ, the concentration of *C. socialis* single cells in the water column was obtained. Fig. 4a–c shows sample in-focus images of *C. socialis* colonies recorded at different depths, while Fig. 5 shows an in-focus colony recorded by the on-board high resolution microscopic holography system. First, the original reconstructed Holosub images of in-focus *C. socialis* colonies were box band-pass filtered to remove the background noise, histogram equalized, and thresholded. Next, the area occupied by the chains and the total size of each colony was mea-

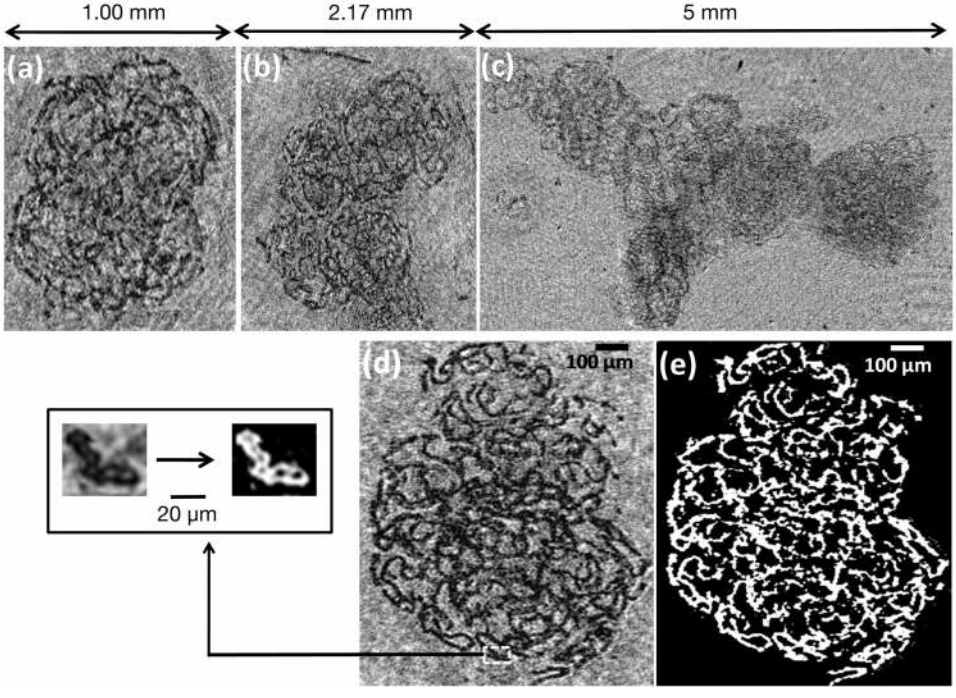

Fig. 4. Sample images of *Chaetoceros socialis* colonies acquired by the Holosub at a depth of (a) 11.96 m, (b) 5.84 m and (c) 4.37 m. The window size is displayed, with the same resolution maintained along the 2 axes. (d,e) Sample in-focus image of a *C. socialis* colony recorded by the Holosub at 6.5 m, and the same image after low-pass filtering, histogram equalization and thresholding used for estimating the number of cells per colony. Inset shows a sub-sample of the *C. socialis* colony, with individual cells visible

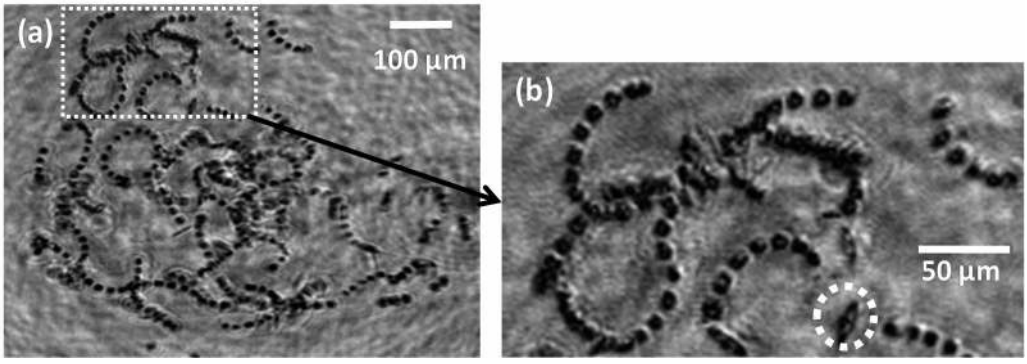

Fig. 5. In focus images of (a) *Chaetoceros socialis* colony, and (b) part of the same colony, magnified (dotted circle: particle that is not *C. socialis*). These data were recorded by the on-board microscopic holographic system using samples collected at 4.5 m

sured. The typical dimensions of individual cells (7 ± 2 µm), as well as the void between cells in the chains, were estimated from the high resolution microscopic holograms, e.g. the one presented in Fig. 5b, where individual cells are clearly discernable. A sample in-focus *C. socialis* colony, from the Holosub data, and the corresponding processed image, used in the cell-count, are illustrated in Fig. 4d,e. The inset shows a sample sub-section of the colony for which individual cells can be identified and counted, numbering 6 for the illustrated sample. Several such sample images, both from the *in situ* (Fig. 4) and the on-board (Fig. 5) holography data, were used to calibrate the parameters relating the cross sectional area of processed images with the corresponding number of cells. The high magnification on-board data provide particularly clear images of individual cells that could be counted and measured (for shape and size), and even used for distinguishing between the *C. socialis* cells and other particles that are mixed with the colony. One such particle is highlighted in the magnified image in Fig. 5b. Then, the total number of cells per colony was calculated based on the area of its processed image. For instance, the estimated number of cells in the colony shown in Fig. 4a is 2150 ± 490. An uncertainty of ~23% was calculated by varying the image enhancement parameters and repeating the analysis for several samples. Fig. 4c shows a large, dense colony found in the thin layer. Here, due to the presence of colonies that occupy substantial thickness, and the resulting degradation of the reference beam, it was frequently difficult to focus on an entire colony in the same plane. Consequently, the internal structure of colonies did not come as clearly into focus as the images at other depths, where colony numbers were lower. For this colony, we estimated the number of cells per colony based on its size and data obtained for other samples. It must be noted that this method provides only a crude cell count, since the cell density in the larger colonies was likely higher than what was calculated, leading to an underestimation of the number of cells. Despite this limitation, the aforementioned framework constitutes a unique approach to obtain the *in situ* abundance of cells in *C. socialis* colonies, accurate at least to an order of magnitude.

Cell counts in collected samples

For the data acquired on board by the 250 frames s^{-1}, high resolution microscopic holography system for the collected samples, 200 holograms were selected for analysis (resulting in a net sample volume of 6 ml), using a sampling frequency of 4 holograms s^{-1} to minimize the likelihood of counting the same object multiple times. An automated particle count was performed by reconstructing each hologram in steps of 20 µm, low-pass filtering the reconstructed images using a 3 × 3 pixel box filter, collapsing them onto a single plane by selecting the lowest intensity for each pixel, and then performing image segmentation to identify the shape (aspect ratio) and size of each object. As a second step, colonies or chains consisting of multiple cells were identified in collapsed images by direct observations, and the constituent number of individual cells was counted visually using images of in-focus colonies/chains, thereby providing a complete cell count. The latter was used to compare the holographic and light microscopy data.

Calculating mean shear and dissipation rates

The absolute velocity in the local flow could not be determined since the Holosub was drifting slowly, but the instantaneous vertical velocity gradients

across the sample volume could be measured. To calculate the velocity relative to the platform at each point, we utilized each of the 9600 and 10 630 low resolution holograms recorded during Ascents I and II, respectively. Each of these holograms were reconstructed in steps of 0.1 mm over a 1.5 cm thick section located at the center of the sample volume, and the images were intensity collapsed onto a single plane. These collapsed images were band-pass filtered to retain only the small particles, and enhanced by histogram equalization. To obtain the local velocity distribution, consecutive images of the 11.5 × 11.5 mm field of view were then divided into interrogation windows of 256 × 256 pixels, and cross-correlated, following standard procedures utilized in Particle Image Velocimetry (PIV) (Adrian & Westerweel 2011). With 50% overlap between interrogation windows, the vector spacing was 0.7 mm, and each instantaneous vector field contained M × N velocity vectors, where M and N varied from 9 to 14. This range was caused by the depth-dependent large mean displacement between consecutive frames, implying that some interrogation windows close to the edge of the field of view did not contain particles that appeared in both frames of the PIV pair. To obtain the characteristic shear, each velocity vector field was divided into an upper and lower half, and the characteristic shear strain rate was calculated from the difference between spatially averaged velocity vectors in the 2 halves. A running average, consisting of 40 consecutively recorded holograms centered around the specified depth, i.e. an average over 2.7 s, or 3 cm in depth, was used to obtain each of the points in the vertical velocity gradient profile, $\partial u/\partial z$, where u is the horizontal velocity and z the vertical coordinate.

In order to facilitate a comparison of the vertical distribution of turbulence level, these data were also used to calculate the turbulent dissipation rate (Pope 2000), which is given by $\varepsilon = 2\nu S_{ij}S_{ij}$. Here ν is the kinematic viscosity and S_{ij} is defined as $S_{ij} = 0.5(\partial u_i/\partial x_j + \partial u_j/\partial x_i)$, where x_i, $i \in [1,2,3]$, denote the 3 spatial coordinates, and u_i the corresponding velocity component. Obtaining an estimate for the dissipation rate from planar velocity distributions requires isotropy assumptions to account for the impact of out-of-plane velocity gradients, as discussed in Luznik et al. (2007). Assuming isotropy, the turbulence dissipation rate estimate is given by $\varepsilon = 15/2\nu\langle(\partial u/\partial z)^2\rangle$. To perform these measurements, the calculations were based on a much thinner sample thickness of 2 mm, and an interrogation window size of 2 × 2 mm. This scale was just above (~1.25 times) the Kolmogorov scale under the present flow conditions, which was sufficient for fully resolving the relevant small-scale velocity gradients (Doron et al. 2001). The local velocity gradients were calculated from the velocity difference between neighboring interrogation windows. A finer scale for these thin samples could not be used since each interrogation window should contain 5 to 10 particles to obtain meaningful data. Each instantaneous velocity distribution provided 56 to 80 data points, where the variable range was once again caused by the depth-dependent large mean displacement between consecutive frames. Averaging over all the points in an instantaneous distribution, and over 40 consecutive realizations provided a profile of the turbulence dissipation rate. Although, such a database cannot be considered as converged turbulence statistics, it nonetheless provided a profile of the characteristic level of turbulence.

Some of the organisms with sparse distributions throughout the water column are shown in Fig. 6. Heterotrophic dinoflagellates of the genus *Noctiluca*, shown in Fig. 6a,b, were found intermittently throughout the water column in small numbers.

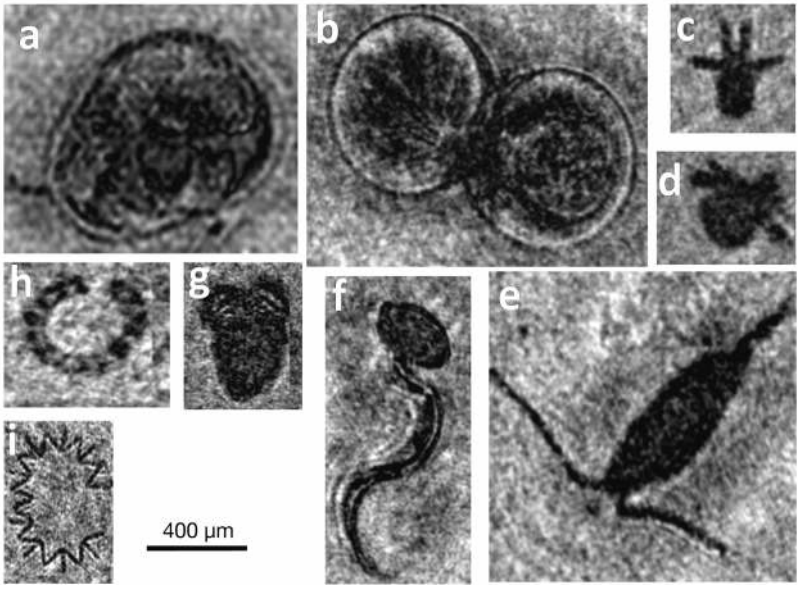

Fig. 6. In-focus images of some organisms found intermittently in the water column. Clockwise, from top left: (a) a single *Noctiluca* cell; (b) a pair of *Noctiluca* cells dividing; (c,d) nauplii; (e) calanoid copepod; (f) appendicularian; (g) a ciliate; (h) *Eucampia zodiacus*; (i) *Thalassionema nitzschioides*. All images have a common scale, as shown

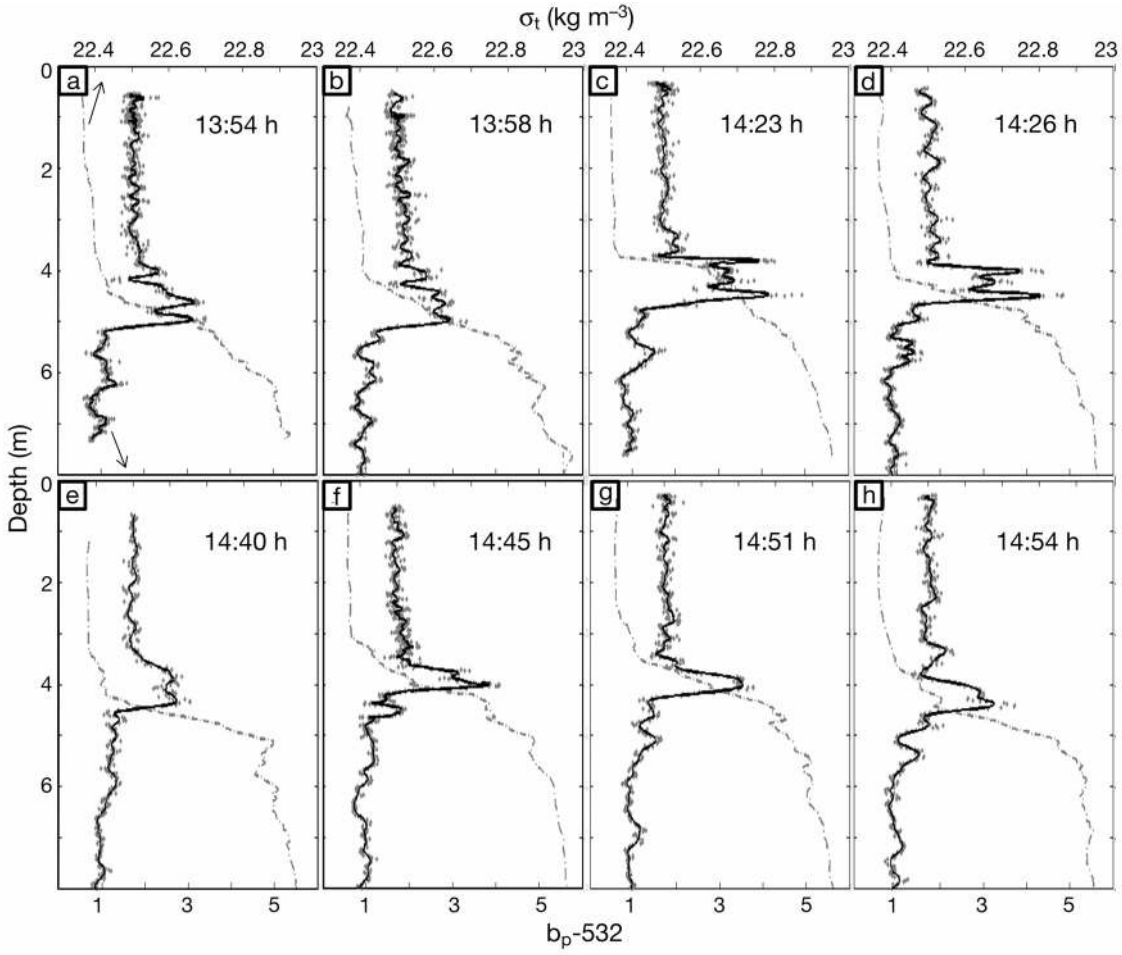

Fig. 7. A time series of vertical profiles of particulate scattering at a wavelength of 532 nm (b_p-532; gray dots and solid black line) superimposed on the profile of density in excess of 10^3 kg m^{-3} (σ_t; gray dashed line), plotted from Multi-Angle Scattering Optical Tool (MASCOT) data. Starting time for each profile is indicated within its panel. Dots represent independent measurements; solid curves represent their 10-point running average. Arrows indicate appropriate horizontal axes for each profile

Appendicularians (Fig. 6f) with a size range of 0.5 to 8 mm were also observed in small numbers at different depths. Other zooplankton, such as copepods and nauplii, shown in Fig. 6c–e, had non-uniform distributions throughout the water column, as discussed in the following sections. Organisms such as ciliates and certain diatom species, shown in Fig. 6g–i, were observed a few times.

RESULTS

Comparison with optical signature profiles

Optical scattering data acquired by the MASCOT were utilized to identify the presence of a thin layer and other patches of elevated particle concentration at the time and location of the Holosub ascents. During these tests, the MASCOT downcasts extended to a depth of ~8 m, while the Holosub recorded data down to 18 m. Since the Holosub was drifting, the distance between these systems varied from several tens of meters to ~100 m based on the length of the optical fiber. Fig. 7a–h shows sample profiles of particulate scattering at a wavelength of 532 nm (b_p-532). As described in Twardowski et al. (2001), b_p, the particle scattering coefficient, is calculated from the volume scattering function $\beta(\theta)$ (sr^{-1}m^{-1}), which is defined as $\beta(\theta) = \mathrm{d}I(\theta)/E\mathrm{d}V$. Here, $\mathrm{d}I(\theta)$ is the scattered intensity in the direction of polar angle θ from the volume $\mathrm{d}V$ and E is the incident irradiance. Integrating the scattering in all directions provides the total scattering coefficient, b (m^{-1}), namely $b = 2\pi\int_0^{\pi}\beta(\theta)\sin(\theta)\mathrm{d}\theta$. In seawater, the scattering coefficient can be divided into its water and particulate components, i.e. $b = b_w + b_p$. The magnitude of b_w is obtained from calibration tests using filtered seawater, and subtracted from b to give b_p, which is representative of scattering by particles >0.2 µm. In each plot of Fig. 7, this quantity is superimposed on the density profiles, which were re-

corded at different times, but at the same location. The measure of density (σ_t) was obtained by subtracting the density of pure water (10^3 kg m^{-3}) from the density of the seawater. For convenience, we will refer to σ_t as density in the rest of the text. This series of profiles indicates the existence of a 0.2 to 1 m deep layer located within a pycnocline, at depths ranging from 3.8 to 4.8 m, with a particulate scattering signature that is substantially higher than that in the rest of the water column. In the cases when the layer is broad, it consists of 2 or more thinner peaks.

We begin by comparing the MASCOT optical profiles to those of the *Chaetoceros socialis* and small particle concentrations, both of which should contribute to the chlorophyll *a* and scattering signatures. Fig. 8a shows the vertical profile of the volume fraction occupied by the *C. socialis* colonies during Ascent II, where each point represents the averaged volume fraction over the instantaneous sample volume of 0.8 × 0.8 × 10 cm^3, and the line represents a 10 point running average. Fig. 8b shows the profile of the mean diameter of *C. socialis* colonies, while Fig. 8c shows the spatially averaged *C. socialis* cell concentrations, calculated as discussed in the previous section. Several *C. socialis* maxima are observed in the depth range of 3.8 to 4.9 m, with the volume fraction, colony size and cell counts all peaking at 4.4 m (dashed line in Fig. 8). At this depth, some of the instantaneous volume fractions exceed 1%, and the mean colony diameters exceed 1.3 mm. Similar numbers have been reported before, e.g. by Alldredge et al. (2002), who observed peak volume fractions of ~0.5% for marine snow aggregates with diameters >0.5 mm.

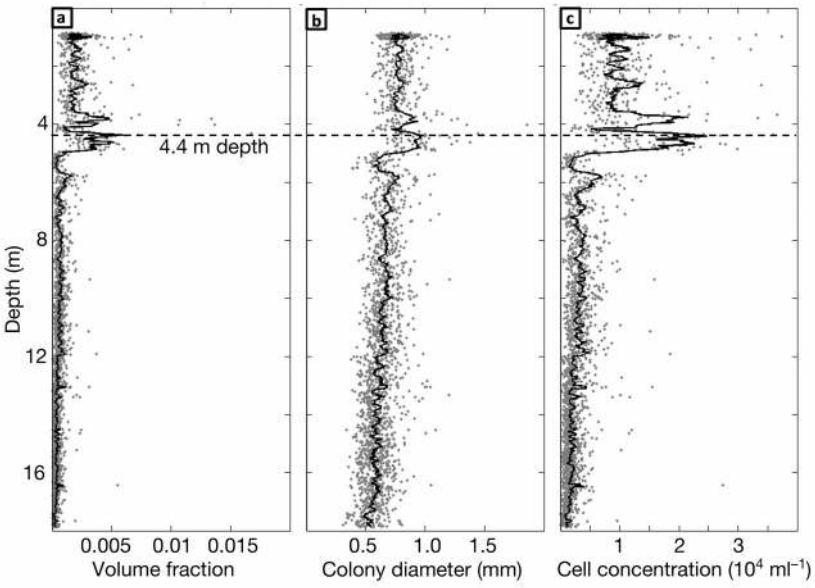

Fig. 8. Depth profile of (a) the volume fraction occupied by *Chaetoceros socialis* colonies in the Holosub sample volume during Ascent II, (b) corresponding colony size, and (c) mean cell concentration. The horizontal dashed line (4.4 m depth) aids in comparing different profiles

Fig. 9d–f compares the vertical profiles of the holographically measured small particle concentration and *Chaetoceros socialis* volume fraction, to those of b_p-532, density and chlorophyll *a* concentration recorded by the MASCOT, during a profile which was temporally closest to Ascent II. It must be noted that due to the (10 to 100 m) distance between sensors, it would be presumptuous to assume that the same layer would appear at the exact same depth at the 2 sites, and the profile comparisons should be interpreted with this in mind. Fig. 9d shows a particle concentration peak at a depth of 4.4 m, whose location matches the lower of the 2 optical signature peaks shown in Fig. 9e,f, the largest *C. socialis* peak and the top of the pycnocline. At depths of 3.8 and 4.7 m, there are peaks in the optical signatures, which coincide with peaks in *C. socialis* volume fraction, though there are no small particle concentration maxima at these depths. Several additional distinct particle maxima appear below the pycnocline, which have been labeled, for convenience, as Layers #1 to #4. Peaks in *C. socialis* volume fraction can be observed to coincide with Layers #1 and #2. Though multiple small peaks in b_p-532 and chlorophyll *a* profiles are also observed at similar depths, they do not match the particle concentration maxima. The same comparison for Ascent I, recorded forty minutes earlier, is presented in Fig. 9a–c. Although the particle concentration peaks are located at different depths (Fig. 9a), the overall picture is similar to the one corresponding to the later ascent. Both the particles and *C. socialis* profiles have multiple peaks, with their respective largest ones coinciding with each other within the (MASCOT) pycnocline. Each profile has another (non-coinciding) large peak just above the pycnocline. The 2 largest small particle concentration maxima at 4.0 and 4.7 m coincide with b_p-532 peaks, but only the lower (pycnocline) peak has corresponding maxima in *C. socialis* and chlorophyll *a* concentrations. The smaller peaks in particle and *C. socialis* concentration at depths of 6.1 and 7.3 m also have corresponding optical signature peaks at similar (but not exactly the same) depths.

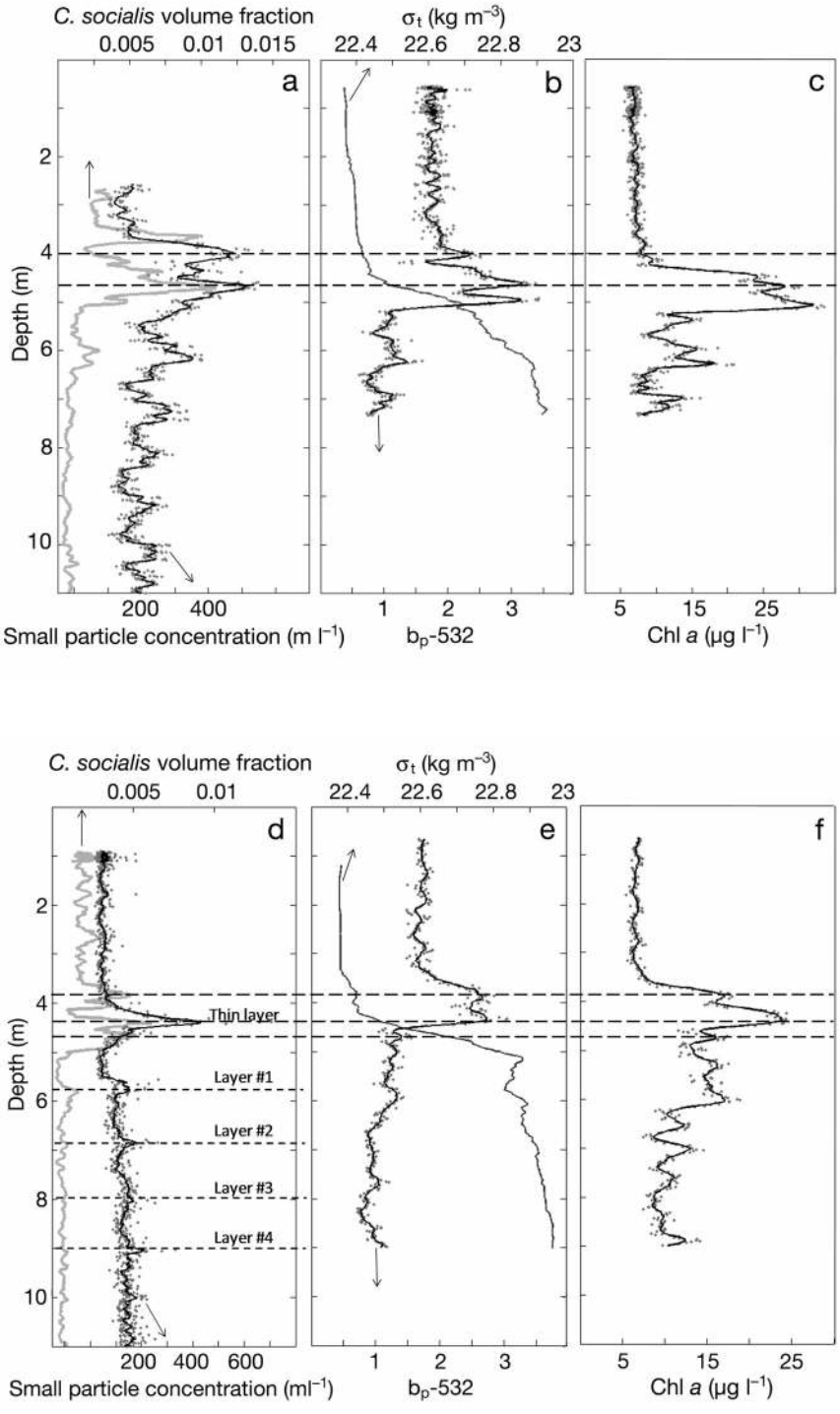

Fig. 9. Profiles of Ascents I (top) and II (bottom): (a,d) holographically measured particle concentration (black line) and *Chaetoceros socialis* volume fraction (gray); (b,e) particle scattering signature at 532 nm (black line and gray dots) superimposed on density (thin gray line); and (c,f) chlorophyll *a* concentration; particle scattering and chlorophyll *a* recorded by the Multi-Angle Scattering Optical Tool (MASCOT) during the deployment that started at 14:40 h. Unlabelled dashed lines: depths of some additional concentration peaks. Dots: independent measurements; solid curves represent their 10-point running average

While Fig. 7 indicates the existence of a 0.2 to 1 m deep persistent layer in the vicinity of the pycnocline, the Holosub data provide independent evidence for the presence of a small particle and *Chaetoceros socialis* colony layer at approximately the same depth, and at a distance of ~50 m away. Data recorded at 14:43 h by a profiler deployed by the URI group ~500 m away (data not shown here) also indicated the presence of a distinct layer with high particulate scattering and chlorophyll *a* concentration located at a depth of 4.3 m in the pycnocline. The spatial-temporal coherence of the layer located at the depth of 4.4 m during Ascent II and 4.7 m during Ascent I suggests that this phenomenon is indeed a thin layer. Coincidence of high particle, *C. socialis* and chlorophyll *a* concentration peaks in this thin layer indicates that it contains an abundance of phytoplankton. The smaller peaks in particle/*C. socialis* concentration below the pycnocline during both ascents, including those identified as Layers #1 to #4 (Fig. 9d), have limited spatial and/or temporal extents that fall below the values typically associated with thin layers (Durham & Stocker 2012). Though not identified as 'thin layers', the local population dynamics and interactions with physical parameters provide insights into the generation and maintenance of inhomogeneities in the water column.

Particle layers and physical parameters

Fig. 10a–d compares the depth profiles of the small particle concentrations superimposed on the *Chaetoceros socialis* volume fraction, with the characteristic shear strain and turbulent dissipation rates, during Ascents I and II. It must be noted that for both ascents, the *C. socialis* colonies dominated the field of view above a depth of 3.8 m, while the small particle concentration was

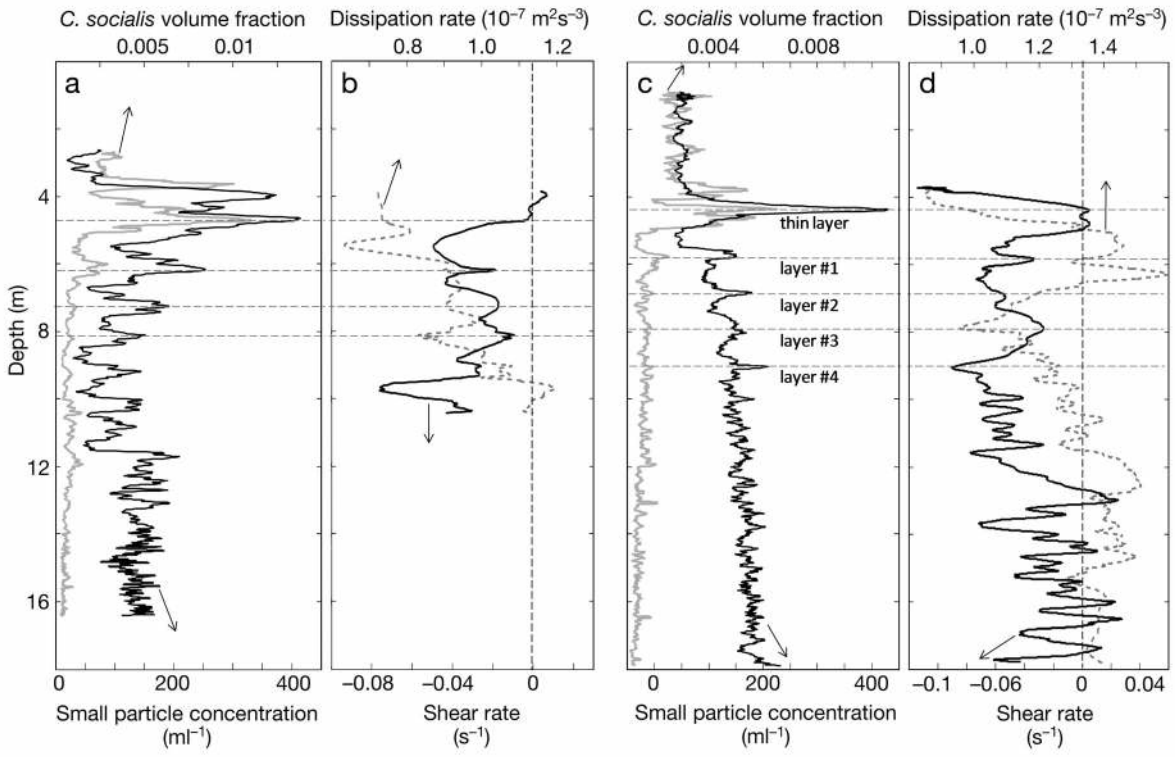

Fig. 10. Vertical profiles recorded during (a,b) Ascent I and (c.d) Ascent II: (a,c) particle concentration (black line) and *Chaetoceros socialis* volume fraction (gray line); (b,d) mean shear rate (black) and dissipation rate (gray dashed line). Vertical dashed lines in panels (b,d) highlight zero shear strain

low, preventing us from obtaining reliable images with uniformly distributed particles to perform PIV analysis, and thus calculate the shear and dissipation rates (Fig. 10b,d).

A comparison of the Ascent II vertical profiles, shown in Fig. 10c,d, indicates that the thin layer, located at the upper part of a strong pycnocline (Fig. 9d–f), coincides with a near-zero shear strain rate region. This region seems to be stably stratified, as the low values of turbulent dissipation indicate. Although we do not have data on density and velocity gradient profiles at the same location to properly estimate the Richardson number ($Ri = (g/\rho)(\partial\rho/\partial z)(\partial u/\partial z)^{-2}$; Woods 1969), MASCOT density and the holographic velocity gradients were used to obtain a rough estimateof $Ri = 15$ at $z = 4.4$ m, well above the critical value of 0.25 required for stable stratification. The *Chaetoceros socialis* volume fraction peak at 3.8 m corresponds to a region of high shear strain, but the stratification and low dissipation rate there again suggest flow stability, consistent with the roughly estimated Richardson number (1.7) there. Below the primary pycnocline, Layers #1, 2 and 3 of Ascent II, with the first 2 coinciding with *C. socialis* peaks, form in narrow regions of local shear strain rate and turbulence minima. We cannot determine, based on the available data, whether the flow is locally stratified. Only the deepest layer (#4) is located in a region of a local shear strain and dissipation rate maximum. The corresponding comparison for Ascent I, shown in Fig. 10a,b, presents consistent trends, namely that both the small particle and *C. socialis* concentration peaks preferentially form at depths with low levels of shear and dissipation rates. To demonstrate this point, we use horizontal dashed lines to show that the 4 particle concentration peaks are located in distinct regions with local shear and dissipation rate minima. The spatial and temporal variability in particle fields seems to be correlated with variation in the shear-strain and dissipation rate fields.

Comparisons with discrete water samples

In order to help with the interpretation of the in situ data, discrete water samples were collected at the URI deployment site at 14:35 h from the surface and at 15:05 h from a depth of ~4.5 m. These samples were analyzed by video microscopy, scanning flow cytometry, microscopic holography, and later by microscopic counts of preserved samples. Though

Table 1. Measured particle concentrations (ml^{-1}) in collected samples and recorded *in situ* by Holosub in East Sound, Washington. 'Chl' and 'non-chl' are particles with and without chlorophyll *a*, respectively. Microscopy-based cell counts used a preserved part of the same sample used for on-board measurements. Na: not available, since the resolution of holograms recorded by the Holosub prevents counting of particles <10 µm. Empty cells indicate that counts do not exist for certain size ranges

Depth (m)	Method	Particle size range							
		4–10 µm		10–20 µm		20–200 µm		>200 µm	
		Chl	Non-chl	Chl	Non-chl	Chl	Non-chl	Chl	Non-chl
On-board measurements from collected samples									
0	Flow cytometer	2095	10065	414	1804	571	1521	82	14
4.5		1370	13864	582	2726	520	2029	54	13
0	Microscopic holography, counting chains/ colonies as a single particle	4143		1138		429		121	
4.5		4748		1329		378		115	
0	Microscopic holography, counting *Chaetoceros socialis* and other diatom cells separately	10130		1119		393		41	
4.5		9740		1306		357		48	
Light microscopy measurements from collected samples									
0	*C. socialis* cells	6780							
4.5		5330							
0	Total cells	7539							
4.5		5964							
Holosub (*in situ*) measurements									
4.5	Total cells	na		354		100		21	
4.5	Estimated *C. socialis* cell concentration	22000 ± 5000							
4.5	Estimated *C. socialis* cell concentration within a colony	$4 \times 10^6 \pm 9 \times 10^5$							

the focus is on the sample collected at 4.5 m, the surface sample aids in determining whether the measured trends are persistent. Table 1 shows the particle counts obtained from the flow cytometer and the on-board holographic microscope at 0 and 4.5 m, cell counts based on light microscopy of preserved samples collected at 0 and 4.5 m, and the *in situ* Holosub data during Ascent II at 4.4 m, i.e. the thin layer. In describing the on-board particle counts, we first compare results obtained by the various instruments using the same collected samples along with species characterization. Then, we compare the on-board to the *in situ* data.

The cytometry counts indicate that while 75 to 80% of the particles <200 µm do not contain chlorophyll *a*, most of the larger particles do. For the holographic microscopy data, we provide several results, the first counts continuous colonies/chains as a single 'particle', and the second, counts each cell separately using the estimation method discussed earlier. Consequently, the number of large particles decreases, and that of small particles increases between counts of colonies/chains and estimated single cell counts (Table 1). For example, for each milliliter of the sample collected at 4.5 m (total sample 6 ml), the 115 objects >200 µm consist of 48 detrital particles, one *C. socialis* colony with ~800 cells, 4 diatom chains consisting of 67 cells in the 10–20 µm range, and 62 diatom chains consisting of 3800 cells in the size range 4–10 µm. Smaller chains are detected as well, with 21 chains in the 20–200 µm size range containing 150 cells in the 4–10 µm range, and 89 chains in the 10–20 µm range consisting of 220 cells in the 4–10 µm range.

For both depths, the holographic microscopy particle counts are about 3 times smaller than flow cytometer data in the 4–10 µm size range, 2 times smaller in the 10–20 µm range, and 5 times smaller in the 20–200 µm range. Above 200 µm, the counts are similar. Possible reasons for these discrepancies, e.g. settling of particles in stationary samples, and associated recommendations for future studies are discussed in detail in the 'Discussion'.

The total particle counts obtained using microscopic holography (10130 ml^{-1} at 0 m and 9740 ml^{-1} at 4.5 m) are of the same order of magnitude as the cell counts from the light microscopy data (7539 ml^{-1} at 0 m and 5964 ml^{-1} at 4.5 m). The latter counts are expected to be lower than the actual cell count, since some fraction of the cells does not survive preservation. A detailed breakdown of the chlorophyll *a* containing species distributions determined using light microscopy is shown in Fig. 11. It is evident that the phytoplankton community within the observable size

range is dominated by diatoms, some of which typically form very large, spherical colonies (*Chaetoceros socialis*), long linear chains (e.g. *Pseudo-nitzschia*, *Chaetoceros vanheurckii*, *Chaetoceros radicans*, *Chaetoceros contortus*), helical chains (*Chaetoceros debilis*) and others that exist as single cells (e.g. *Cylindrotheca closterium*, various pennate diatom species). The on-board cinematic holographic microscopy data are consistent with these findings, showing that a majority of the observed cells are passively advected rather than display swimming motions. The holographic microscopy samples contain only one dinoflagellate from the genus *Protoperidinium*, and a few larger (30 to 80 µm) ciliates, particularly *Myrionecta rubra*, that swim intermittently at speeds reaching 2.5 cm s^{-1}.

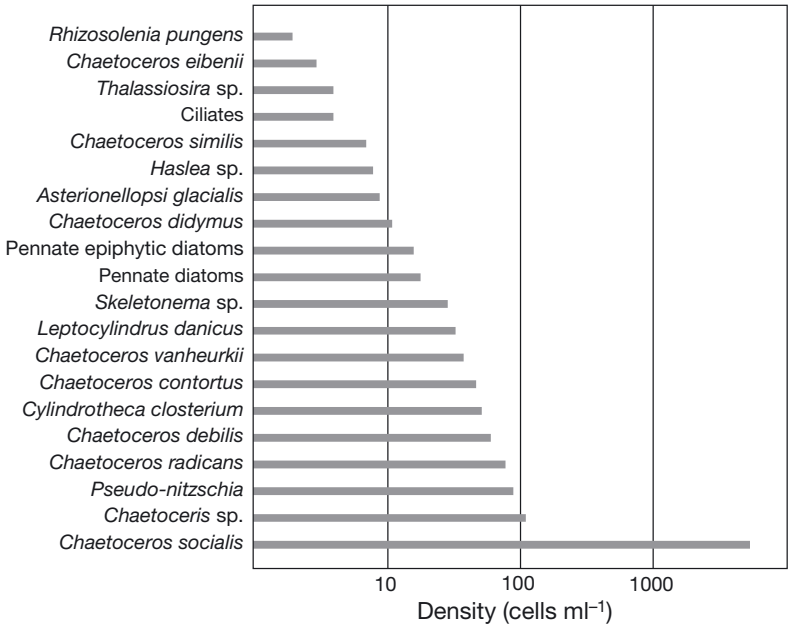

Fig. 11. Species counts obtained from microscopic visual counts performed in the lab. The observed sample was collected at 4.5 m depth during the same deployment as the Holosub study was carried out, and preserved for subsequent analysis. The *x*-axis is log scaled

The particle concentrations acquired by the Holosub (Table 1) are significantly lower than those acquired by both the on-board holographic microscopy and cytometry data. We attempt to explain these trends and associated implications in the discussion section, including differences in location and resolution issues. Table 1 also provides an estimate of *in situ Chaetoceros socialis* cell concentrations in the thin layer, i.e. 22 000 ± 5000 ml^{-1}. This value is higher but of the same order of magnitude as the on-board holographic count of all the particles, and is higher than the microscopy based cell counts, which, as discussed above, is affected by preservation. Within the volume occupied by the colonies, the cell concentrations are 2 orders of magnitude higher than the averaged values, reaching 4×10^6 ml^{-1} (Table 1).

Diatom chain length and orientation *in situ*

The images of predominantly chain-forming diatom species in samples collected at a depth of 4.5 m (Fig. 12), ~500 m from the Holosub, primarily include linear chains belonging to the genus *Chaetoceros*, and helical chains, primarily of the species *C. debilis*. We cannot identify the long chains in the Holosub data. During Ascent II, the running average diatom chain lengths generally (but not monotonically) decrease from 1.4 to 0.5 mm with increasing depth (Fig. 13b), but the observed sizes of individual chains reach to 8 mm. For the entire volume above the pycnocline, the chains are characteristically longer than those at depths below. The number of diatom chains more than doubles as the depth decreases from 9 to 5 m, peaking at 3.5 ml^{-1} (4.3 for an individual case) at 5 m, i.e. clearly below the thin layer and below the *C. socialis* maxima. Chain numbers remain

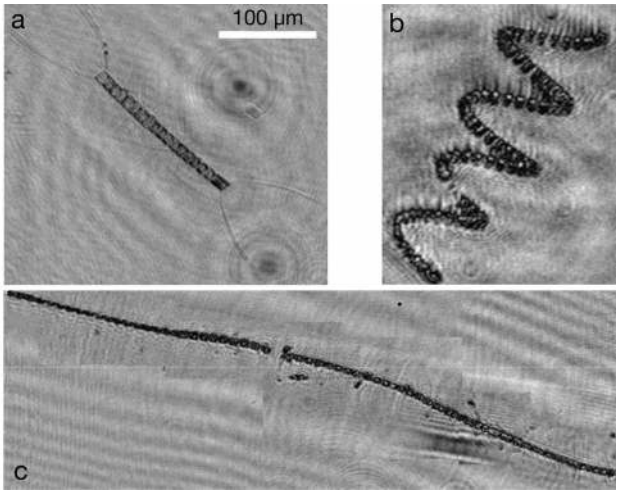

Fig. 12. Samples of predominant chain-forming diatom species: (a) *Chaetoceros vanheurckii* linear chain; (b) *C. debilis* forming a helical chain; (c) *C. radicans* linear chain. In-focus images are obtained from holograms recorded on-board by the microscopic holographic system, from samples collected at 4.5 m depth

high, but at a slightly lower level than the peak, all the way to the surface (Fig. 13c). Their angles of inclination with the horizontal direction (Fig. 13a) decrease significantly in the vicinity of the thin layer, where, as noted before, the shear strain and turbulence rates are low and the density gradients are high, as illustrated in Fig. 13a–c. The upper part of the broad low inclination region, between 3.8 and 4.4 m, coincides with a region of low turbulence. Diatom chain orientation angle remains low over the entire domain of low shear below the inclination minimum. There are several other narrow regions in the water column where the orientation angle, shear strain and turbulence minima coincide, which are marked by thick dotted lines in Fig. 13. Interestingly, these regions are also characterized by increased gradients in diatom abundances, which, as discussed in the discussion section, might be related to the dependence of settling velocity on chain orientation. Conversely, some (but not all) depths with local shear and turbulence maxima (marked by thin dashed lines) contain diatom chains with higher inclination angles compared to those in their surrounding areas. To illustrate this variability in orientation, Fig. 14 provides sample in-focus, high resolution Holosub images of diatom chains. The diatoms located in the stably stratified thin layer are aligned almost horizontally (Fig. 14a), but the inclination increases progressively, and at a depth of 5.74 m (Fig. 14c), where there is a local maximum in shear strain rate, most of the diatom chains appear to be nearly vertical. For Ascent I, Fig. 15 only provides a comparison between the diatom chain orientation and the mean shear that confirms the consistency in alignment trends with the

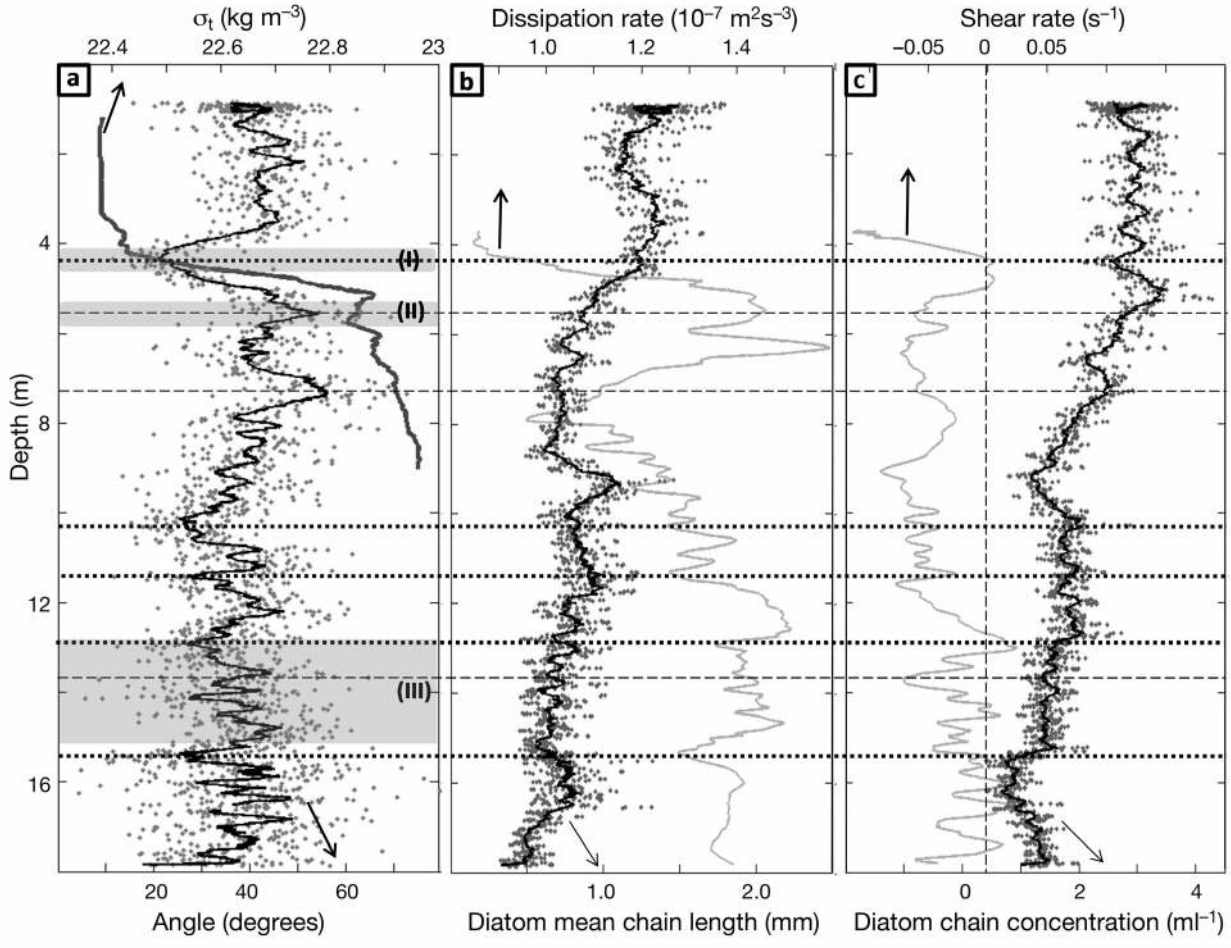

Fig. 13. Profiles of (a) diatom chain orientation (black line and gray dots) and density (dark gray line); (b) mean diatom chain length (black line & gray dots) and dissipation rate (gray line); (c) diatom chain concentration (black line and gray dots) and mean shear rate (gray line). The Holosub data are from Ascent II, and density data are from the Multi-Angle Scattering Optical Tool (MASCOT) deployment that started at 14:40 h. Dotted horizontal lines indicate depths of low diatom chain inclinations. Horizontal dashed lines: regions with elevated inclinations; vertical dashed line: zero shear rate. Shaded areas: depth regions (Regions I, II and III) used for analysis of diatom chain inclinations (see Fig. 17)

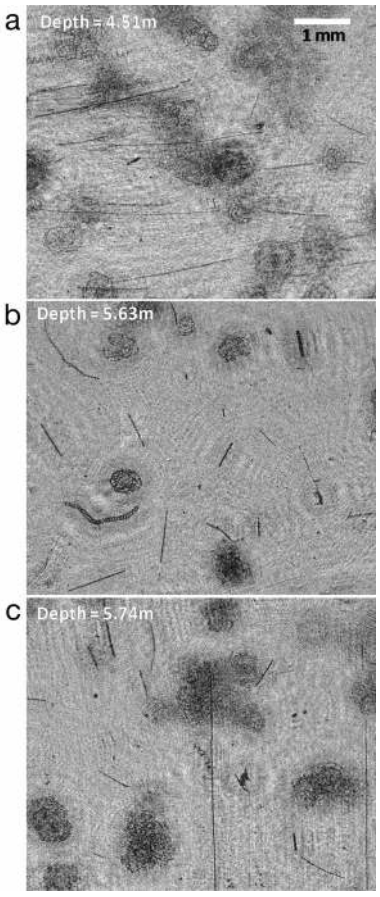

Fig. 14. Sample in-focus reconstructed images of diatom chains at (a) 4.51 m, (b) 5.63 m, and (c) 5.74 m depth, each showing a field of view of 6.24 × 5.8 mm^2. Note the presence of *Chaetoceros socialis* colonies in the background, some of them out of focus

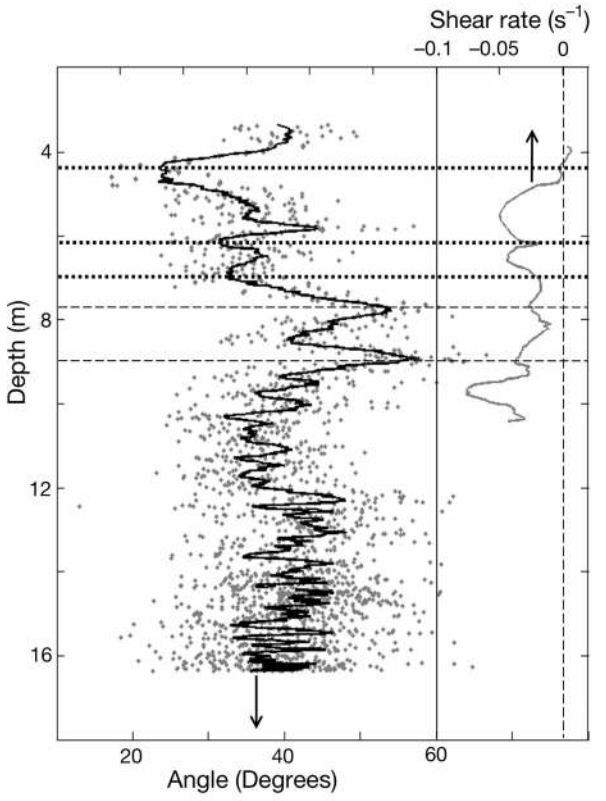

Fig. 15. Profiles of diatom chain orientation (black line and gray dots) and mean shear rate (gray line) for Ascent I. Dotted and dashed lines: depths of low and high diatom chain inclinations, respectively

results obtained for the later ascent. The smallest angle and broadest minimum occur in the near zero shear rate region in the pycnocline, and several other minima coincide with local shear troughs. Conversely, the angles peak at depths of local shear maxima. As for the correlation with the dissipation rate (Fig. 10b), in general, the angle minima occur in regions of low dissipation, but the correspondence to alignment trends is not as distinct since the dissipation is lower everywhere compared to the later ascent. Other (not shown) trends of Ascent I include a distinct maximum in mean chain length (1.5 mm) at the top of the pycnocline, coinciding with the angle minimum, and characteristic concentrations that do not differ significantly from those of the later measurements.

It must be noted that measurements of diatom orientations and lengths are based on the 2-dimensional (2D) projection of 3D orientation. Thus, the lengths of the diatom chains are underestimated. Furthermore, nearly horizontal diatom chains may appear vertical if they are inclined primarily out of plane, introducing a bias in the measured angles, as quantified in Fig. 16, which shows the probability distribution function (PDF) of the 2D projection angle for lines with random 3D orientations. To obtain this distribution, we consider a line oriented in 3D at polar angle θ_p ($0 < \theta_p < \pi$) and azimuthal angle φ_p ($0 < \varphi_p < 2\pi$). Its 2D projected angle is given by $\tan^{-1}(|\tan\theta_p/\cos\varphi_p|)$. If both θ_p and φ_p are uniformly distributed, i.e. the particle 3D orientation is random, the PDF of $\tan^{-1}(|\tan\theta_p/\cos\varphi_p|)$ has the form shown in Fig. 16. The measured PDFs of 2D orientation angles of diatom chains are presented as scatter plots in Fig. 17. The solid lines show the exponentially least-square fitted distribution of the original data. To demonstrate how they differ from the random PDF (Fig. 16), we divide the measured distributions by the random one at each (projected) angle, and then renormalize the result to have a cumulative value (area under the graph) of one. The renormalized ratios are plotted as dashed lines in Fig. 17, and referred to as 'corrected' PDFs. The first 2 plots show orientation distributions in sample volumes in depth bands of 0.2 m centered around specified values, one denoted in Region I in Fig. 13, centered around 4.4 m depth, where the angle, shear strain and turbulence are low (Fig. 17a); and the other in Region II, cen-

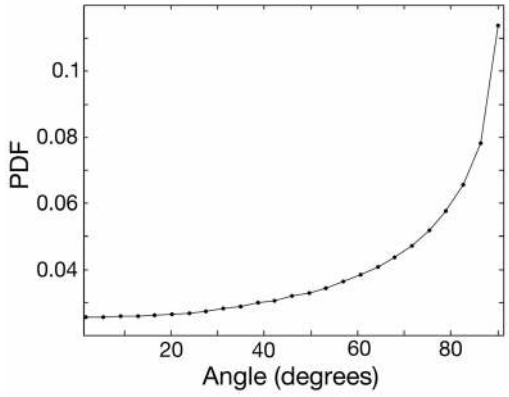

Fig. 16. The orientation distribution function (ODF), i.e. the probability distribution function (PDF) of the angle of inclination of planar projections of randomly distributed 3D lines

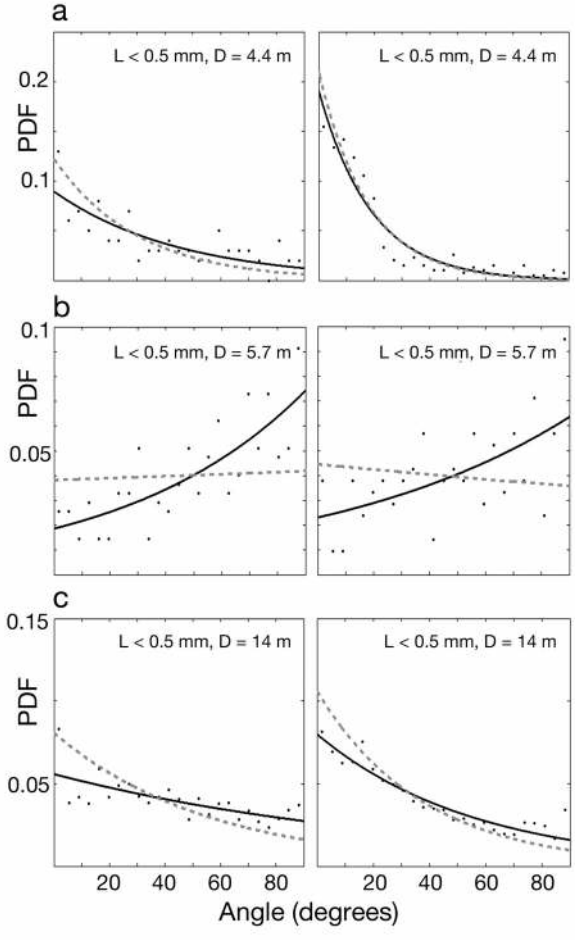

Fig. 17. Probability distribution functions (PDFs) of 2D projections of diatom chain inclination angles recorded by Holosub Ascent II in Region I, II and III, as shown in Fig. 14: (a) Region I, depth band 0.2 m, centered around 4.4 m; (b) Region II, depth band 0.2 m, centered around 5.7 m; (c) Region III, depth band 2.0 m, centered around 14 m. Adjusted PDFs (gray dashed line) are superimposed for comparison (see text for further explanation). L: diatom chain length; the left and right columns show results for short (L < 0.5 mm) and long (L > 0.5) diatoms chains respectively. D: depth

tered around 5.7 m depth (Fig. 17b), where the angle, strain and turbulence are high. The third PDF (Fig. 17c) covers a broad depth band of 2 m, centered around 14 m depth, shown as Region III in Fig. 13, and serves as a reference. Dividing the database into chains shorter and longer than 0.5 mm length, shown in the left and right sides of Fig. 17, respectively, indicates that while in regions of high shear there is no significant length-dependent difference in orientation, in the rest of the water column, the longer chains have a higher tendency to be aligned horizontally. We reiterate that the lengths are based on 2D projections on the camera plane, due to which some of the chains that are classified as <0.5 mm might actually be longer.

To verify that the chain orientations are indeed non-random in regions of moderate to low shear, we use the Pearson's chi-squared test (Pearson 1900), which is performed on the null hypothesis that there is no significant difference between the random orientation distribution function (ODF) and the measured PDFs for Ascent II. Table 2 lists the chi-squared statistics for the 3 sample depths shown in Fig. 17, and the corresponding p-values for data histograms divided to 25 bins. These p-values indicate that at depths of 4.4 m and the broad region surrounding 14 m, the null hypothesis can be rejected, implying that the distributions at these depths are significantly different from the random ODF. On the other hand, at 5.7 m, where there is a local maximum in shear and dissipation, the p-value indicates that the measured distribution is not statistically different from the ODF of randomly aligned diatom chains.

One should keep in mind that due to the bias shown in Fig. 16, the actual distribution of 3D orientation in the low shear region should have a higher tendency towards low angles compared to the measured results, as indicated by the corrected values shown in dashed gray lines in Fig. 17. Reasons for this preferred alignment are analyzed in the discussion.

Table 2. Chi-squared statistics (χ^2) and corresponding p-values for the comparison between orientation of diatom chains shown in Fig. 18 and random orientation distribution function (ODF) presented in Fig. 17

Depth (m)	Diatom chain length			
	<0.5 mm		>0.5 mm	
	χ^2	p	χ^2	p
4.4	101.5	2×10^{-6}	1108.6	4×10^{-14}
5.7	32.1	0.124	22.1	0.574
14	97.0	7×10^{-7}	315.4	1×10^{-9}

Zooplankton distribution *in situ*

Fig. 19 shows the vertical distribution of zooplankton, consisting of copepods and nauplii with a size range of 0.2 to 1.5 mm, superimposed on the small particle concentration and *Chaetoceros socialis* volume fraction for the 2 ascents. Each zooplankton concentration data point is a result of averaging over 20 holograms, equivalent to a sampling volume of 130 ml, a volume significantly smaller than those typically utilized in zooplankton statistics (tens of liters). Thus, the zooplankton distribution cannot be considered as statistically convergent. However, such a distribution can still indicate trends, which might help elucidate predator-prey interactions (Fig. 18). In Fig. 18b, it is evident that the thin layer and particle Layers #1 and #4 coincide with troughs in zooplankton concentration, while the Layers #2 and #3 are located in an area of low numbers of zooplankton, just below a zooplankton peak. The multiple peaks with high *C. socialis* concentrations (3.8 to 4.9 m), in and above the pycnocline, correspond to a zooplankton concentration trough, while at lower depths, 2 of the discernable peaks in *C. socialis* volume fraction also correspond to minima in predator concentration. However, the trends are not as consistent in Fig. 18a. Avoidance still seems to occur in the vicinity of the primary particle peaks at 3.8 and 4.7 m along with several of the deeper peaks that are marked by horizontal dashed lines. However, it does not occur at other depths that are marked by dotted lines.

DISCUSSION

Simultaneous in situ measurements in East Sound, Washington, involving the Holosub and hydrographic-optical profilers, as well as analysis of samples using flow cytometry, holographic and light microscopy, enabled us to examine interactions among biological, physical and optical parameters in the water column. To perform this study, we introduced several new data analysis techniques for estimating the concentration of cells in a *Chaetoceros socialis* colony, the vertical gradients of horizontal velocity, the turbulent dissipation rate, and orientation of diatoms. We also adapted procedures described in Katz & Sheng (2010) to measure the concentration and spatial distribution of particles. Several trends, some of which are new, and others consistent with previous findings, were observed based on multiple deployments of the MASCOT optical profiler, and detailed analysis of 2 datasets recorded during 2 Holosub ascents separated by 40 min, the first containing 7500 holograms (Ascent I), and the second 12 500 holograms (Ascent II).

While prior studies, e.g. Alldredge et al. (2002), measured marine snow, phytoplankton, and zooplankton distributions, and turbulent dissipation, they involved use of multiple profilers sampling different volumes, and collection of samples for subsequent microscopic analysis. The turbulence parameters were determined indirectly, e.g. the dissipation rate was estimated by fitting the measured temperature power spectra to the Batchelor's model spectrum (Gibson & Schwarz 1963). As noted before, Alldredge et al. (2002) already showed the correlation among thin layers with high particle concentration, presence of a pycnocline, and low turbulence levels. They also showed that zooplankton avoid layers containing high concentration of marine snow. Digital hologra-

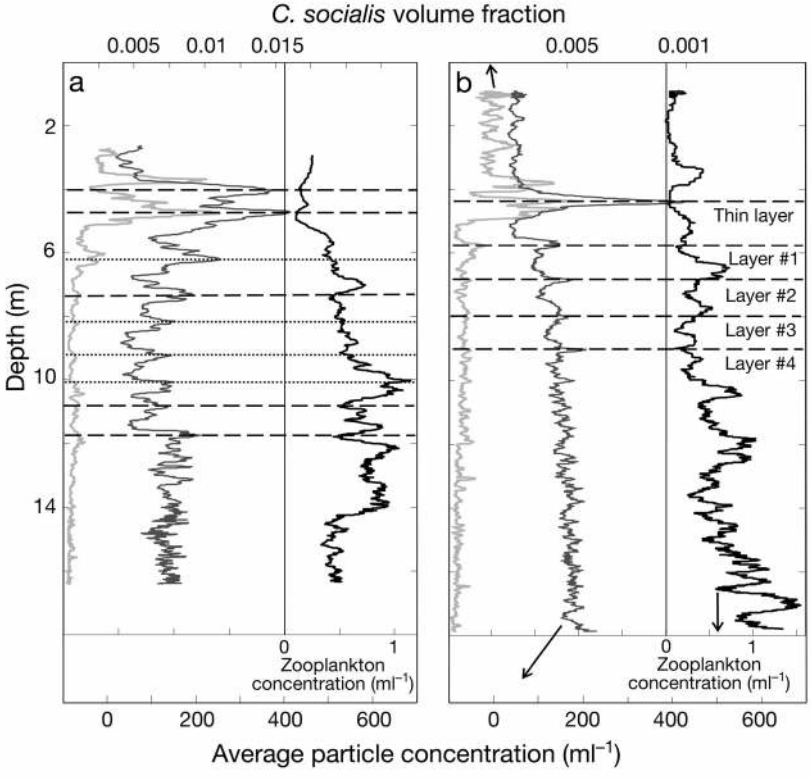

Fig. 18. Depth profiles of zooplankton concentration (black line) superimposed on the small particle concentration (dark gray line) and *Chaetoceros socialis* volume fraction (light gray line) for (a) Ascent I and (b) Ascent II. Horizontal dashed and dotted lines mark layers with elevated particle concentrations

phy and the procedures introduced in this paper enabled us to determine the spatial structure of particle aggregations as well as the (directly measured) local shear and turbulence to which they are exposed to *in situ*. As a result, we revealed several distinct, fine-scale correlations among physical parameters, population and orientation of particles. For example, we determined the effect of local shear on the alignment of diatom chains, as well as the scales, number and structure of the large *Chaetoceros socialis* colonies. These unique results are discussed below in 4 separate sections, each focusing on a different topic.

Presence and formation of inhomogeneities, including a thin layer

The results demonstrated that a number of layers with elevated concentrations of small particles developed in the water column. A thin layer with substantial temporal and spatial coherence was identified at the upper part of a strong pycnocline. Additional distinct particle peaks located deeper in the water column could not be identified as broad thin layers since they did not have corresponding signatures from the optical sensors. Though a complete time history of these layers and associated physical parameters would be necessary for a full understanding of factors controlling their formation and persistence, analysis of the current dataset identified several trends. The thin layer was associated with a stably stratified shear layer with low dissipation. These observations are consistent with field data of, e.g. Sullivan et al. (2010a), which showed that a majority of thin layer formation occur in the vicinity of pycnoclines. They also agree with the conclusions of Prairie et al. (2001) that sharper phytoplankton concentration gradients, i.e. narrower layers, co-occur with low mixing and sharp density gradients. Some of the *Chaetoceros socialis* colony peaks coincided with the broad thin layer as well as several of the particle layers, but the water column contained several *C. socialis* colony peaks without small particle maxima at those depths. Both the small particle and *C. socialis* peaks were preferentially located in regions of low shear strain and dissipation rates, namely, in layers with reductions in both turbulence-induced erosion and mixing with the surrounding volume.

The physical mechanisms typically attributed to formation of inhomogeneities, summarized in Stacey et al. (2007), include straining of a phytoplankton patch (Osborn 1998), motility disruption by shear (Durham et al. 2009), and buoyancy-induced restoring forces (Franks 1992). Since the particles within the thin layer consisted predominantly of non-motile diatom cells and particles without chlorophyll *a* content, motility-based mechanisms were ruled out. Buoyancy effects, namely retention of particles along an isopycnal of equal density, might have contributed to the formation of the thin layer, since the thin layer was associated with the predominant pycnocline. It is not obvious how the particle layers located below the pycnocline formed in the first place, and whether the high strain rates bordering them played a role in their formation by shearing an initially homogeneous phytoplankton patch (Birch et al. 2008). One possible scenario is that a minimum in shear rate encouraged the local formation of *Chaetoceros socialis* blooms, which in turn acted as a deterrent for grazing by zooplankton, allowing smaller phytoplankton to grow. Indeed, simultaneous peaking of *C. socialis* and small particle concentrations, along with a low concentration of predators, was observed at several depths with low shear strain and turbulence levels. They occurred during both of the Holosub ascents in the thin layer and in multiple additional transient layers below it.

Orientation of diatom chains

Our results indicated that the diatom chains clearly tended towards a horizontal alignment, except for regions with high shear strain rate. This preference can be explained by Jeffery's (1992) theory of the motion of spheroids in a shear flow. In a low Reynolds number uniform shear flow, spheroids undergo periodic rotations when they are perturbed from a horizontal equilibrium orientation. Their angular velocity ω, and period of rotation T, are given by

$$\omega = \mathrm{d}\varphi/\mathrm{d}t = G(\sin^2\varphi + \cos^2\varphi/r^2);\ T = 2\pi r/G \qquad (1)$$

where t is time, φ is the inclination angle, G is the shear strain rate, and r the length ratio of the long to short axes ($r \gg 1$). Eq. (1) reveals that the angular velocity is minimal for φ = 0, implying that a large fraction of the rotational period is spent in alignments close to those of the local streamlines, i.e. horizontal. The shape of many marine planktonic diatoms deviates from the spheroids used for developing Eq. (1), and they are exposed to varying shear rates and turbulence levels. Shape effects reduce the periods of rotation, though the functional dependence on G and r remains consistent with that in Eq. (1) (Karp-Boss & Jumars 1998). Turbulence should presumably randomize the chain orientation. Indeed, in some, but

not all of the regions of high shear and dissipation rates, the orientation distributions became nearly random (Fig. 17b). Conversely, in regions of low shear and dissipation, the orientation became preferentially horizontal, consistent with the implications of Eq. (1). The statistical significance of the latter observation is confirmed using the Pearson's chi-squared test. Furthermore, except for regions of high shear and turbulence, the longer chains showed a higher tendency to be nearly horizontally aligned compared to shorter chains, also consistent with Eq. (1). Thus, despite the simplifying assumptions, Jeffery's model predicts trends that are consistent with our observations of the *in situ* orientation of diatom chains. Interestingly, a recent study by Marcos et al. (2011) used experimentation and modeling to show that at a much smaller scale, elongated microbes subjected to a laminar shear are also preferentially aligned along the flow direction.

Slow sinking of diatom chains in the water column can also explain the aforementioned preferential orientation, though the *in situ* measurements in this study could not establish whether the diatom chains were indeed negatively buoyant. Previous studies (Padisak et al. 2003) showed that rigid cylinders, with dimensions and specific gravity similar to those of diatom chains, maintain their orientation while sinking slowly (Stokes flow) in a quiescent flow. Furthermore, the sinking speed decreased significantly with decreasing orientation angle and increasing aspect ratio. A lower sinking speed presumably implies longer time of flight through a certain region, and consequently a preferential accumulation of chains with low inclination angles in regions of low shear, which is more pronounced for long chains. This reasoning is consistent with the predominantly near-horizontal orientation near the thin layer as well as in other areas of shear/dissipation minima. However, there was no evidence of accumulation in regions of low shear. In fact, several minima in inclination angle seemed to coincide with or were located just below (~0.1 m) concentration gradients (Fig. 13), suggesting that further factors were involved, e.g. effects of turbulence on settling rates.

Non-random alignment of diatom chains within the water column has critical repercussions to the ambient light field and associated inherent optical properties. When non-spherical particles are preferentially aligned, they can affect the volume scattering function, particularly by an enhancement of backscattering (b_b) (Marcos et al. 2011). This phenomenon could have repercussions to remote sensing products, where the reflectance is approximately proportional to $b_b/(a + b_b)$ (Gordon et al. 1975), a being the absorption coefficient. Further, overall light transmission through the water column may be affected, potentially changing local phytoplankton growth dynamics. To the best of our knowledge, this study is the first demonstration of preferential alignment by large colonial phytoplankton in a natural environment, along with simultaneous direct measurements of shear strain and dissipation rates.

Predator–prey interactions

In both ascents, the thin layer with high particle and *Chaetoceros socialis* colony concentrations in the vicinity of the pycnocline exhibited a low concentration of zooplankton. The zooplankton also seemed to avoid the other layers with elevated particle concentration of Ascent II, and several, but not all, of the particle peaks of Ascent I. Avoidance of high concentration phytoplankton layers by zooplankton is consistent with the findings of Holliday et al. (2003), who reported that the copepod *Acartia tonsa* accumulates on either side of chlorophyll *a* layers, and that mysid shrimp avoids thin layers of *Chaetoceros socialis*. Also, Fiedler's (1982) sampling based field study showed that macro-zooplankton avoid phytoplankton layers, while field data reported in Sullivan et al. (2010a) indicated that the chlorophyll *a* biomass in thin layers has a consistently lower rate of depletion compared to the rest of the water column. These observations suggest that at least in some cases, layers with high particle concentration may deter grazing.

Comparisons involving on-board discrete water samples

There are a number of possible reasons for the discrepancies between the particle counts obtained using cytometry and on-board holographic microscopy. For both the surface and 4.5 m deep samples, the flow cytometry results were consistently higher, but of the same order of magnitude as those of holographic microscopy. Since both sets showed similar trends, we assume that the discrepancy was not caused by variations among sub-samples used for the different techniques. Furthermore, since the discrepancy extended to the 20–200 µm range, for which the reconstructed particle images already occupied at least 12 × 12 pixels, and the images were clear and showed distinct shapes, it is unlikely that the discrepancy was caused by resolution limits of the holography system. To verify this statement, we compared

the variations in concentration with distance from the hologram plane, which affected the resolution for small particles (Sheng et al. 2006). The results, based on analysis of 500 holograms, showed a mean decrease in concentration of ~1% for every millimeter of distance from the hologram plane for particles <10 µm, and a negligible decrease for larger ones. Thus, resolution limits for small particles were also unlikely to cause the discrepancy. A possible explanation for this difference might have been the settling of non-neutrally buoyant particles in the stationary water samples placed in the cuvette, as it lay undisturbed for ~15 min before we recorded the holograms. Recent laboratory observation confirmed that settling of 10 µm particles in stationary samples indeed reduced the number of particles in the middle of the sample volume with time. For future studies, gentle circulation can solve this problem.

There are several possible reasons for the discrepancy between the particle counts acquired by the Holosub and those based on the sample collected at ~4.5 m. First, the measurements were performed at sites located >500 m apart. Second, the lower magnification, 3.9 µm pixel^{-1}, should severely affect the ability to detect particles <10 µm, and to some extent up to 20 µm, especially with increasing distance from the hologram plane. Based on the measured variations in the particle concentration with distance from the hologram plane in the *in situ* results, using data from 100 holograms, the average decrease in counts for 10–20 µm particles was 0.17% mm^{-1}. For a 10 cm deep sample, this signal attenuation caused an average loss of data of 13.5%. For particles >20 µm, the signal attenuation was negligible. Thus, attenuation of signal was a contributor, but not to the level that would explain the discrepancy between the *in situ* and on-board microscopic analysis. Third, compared to the Holosub, which counted particles in their natural state with minimal disturbance, the sample collection and subsequent analysis might have caused some breakage, especially for the large colonies, chains and brittle detrital particles. Such breakage would increase the particle counts. Indeed, the samples of *Chaetoceros socialis* colonies examined holographically on board appeared to be significantly smaller than the *in situ* colonies, and had multiple broken cell linkages, as seen in Fig. 5a. However, unbroken large colonies were also observed in the collected samples, and as a result, the impact of breakage on the counts is not clear. Finally, the on-board samples showed that the space occupied by the large *C. socialis* colonies also contained many small particles, which were not part of the colony itself. Thus, they were not accounted for in the analysis of *in situ* data. Once the samples were collected, and the colony became partially fragmented, at least some of these particles became dispersed in the sample volume and were counted separately.

The present study has taught us that some of the procedures should be modified in future studies. For example, the resolution of the *in situ* holograms, at least for one of the views, should be increased to about 1 µm pixel^{-1}. Also, the water samples used for microscopic observations and taxonomy should be collected at the same time and location as the *in situ* studies, and during the on-board holographic imaging, the sample must be constantly agitated to prevent settling of particles. Sampling of the water by the CTD should be performed at the same elevation as the sample volume. Having a velocity sensor on board, such as an ADV to measure the platform motion relative to the local flow would also be beneficial. We have already deployed the system together with an ADV, but only when it was used in a profiling mode.

Finally, this analysis demonstrates that because of the complex environments inherent to the coastal ocean, an increased understanding on the causes and effects associated with spatial distributions of particles and organisms is greatly enhanced by the simultaneous deployment of multiple complementing instruments that resolve the physics, chemistry and biology in space and time, and resolve particles in their undisturbed, natural state.

Acknowledgements. This research was sponsored by the NOPP program and the Office of Naval Research (award numbers N0001410C0041 and N000140910492). We thank our program officers, Steve Ackleson and Joan Cleveland. The authors also thank Yury Ronzhes and Steven King for their invaluable technical support and contributions in assembling and deploying the Holosub. Thanks are also due to Ed Malkiel and Woody Pfitsch, who designed and assembled the Holosub several years ago, for their support during early phases of reassembling the system. Finally, we thank our colleagues who assisted in the East Sound field exercise, Jim Churnside of NOAA, Alan Weidemann of NRL, and Scott Freeman and Heather Groundwater of WET Labs.

LITERATURE CITED

Adrian RJ, Westerweel J 2011. Particle image velocimetry, 1st edn. Cambridge University Press, New York, NY

Alldredge AL, Cowles TJ, MacIntyre S, Rines JEB and others (2002) Occurrence and mechanisms of formation of a dramatic thin layer of marine snow in a shallow Pacific fjord. Mar Ecol Prog Ser 233:1–12

Benoit-Bird KJ, Moline MA, Waluk CM, Robbins IC (2010) Integrated measurements of acoustical and optical thin

layers. I. Vertical scales of association. Cont Shelf Res 30: 17–28

Birch DA, Young WR, Franks PJS (2008) Thin layers of plankton: formation by shear and death by diffusion. Deep-Sea Res 55:277–295

Carder KL (1979) Holographic micro velocimeter for use in studying ocean particle dynamics. Opt Eng 18:524–525

Cassie RM (1963) Micro-distribution of plankton. Oceanogr Mar Biol Annu Rev 1:223–253

Churnside JH, Donaghay PL (2009) Thin scattering layers observed by airborne lidar. ICES J Mar Sci 66:1–12

Cowles TJ, Desiderio RA, Carr ME (1998) Small-scale planktonic structure: persistence and trophic consequences. Oceanogaphy 11:4–9

Davis CS, Gallanger SM, Berman MS, Haury LR, Strickler JR (1992) The Video Plankton Recorder (VPR): design and initial results. Arch Hydrobiol Beih 36:67–81

Dekshenieks MM, Donaghay PL, Sullivan JM, Rines JEB, Osborn TR, Twardowski MS (2001) Temporal and spatial occurrence of thin phytoplankton layers in relation to physical processes. Mar Ecol Prog Ser 223:61–71

Derenbach JB, Astheimer H, Hansen HP, Leach H (1979) Vertical microscale distribution of phytoplankton in relation to the thermocline. Mar Ecol Prog Ser 1:187–193

Donaghay PL, Osborn TR (1997) Toward a theory of biological-physical control of harmful algal bloom dynamics and impacts. Limnol Oceanogr 42:1283–1296

Donaghay PL, Rines HM, Sieburth JM (1992) Simultaneous sampling of fine scale biological, chemical and physical structure in stratified waters. Arch Hydrobiol 36:97–108

Doron P, Bertuccioli LL, Katz J, Osborn TR (2001) Turbulence characteristics and dissipation estimates in the coastal ocean bottom boundary layer from PIV data. J Phys Oceanogr 31:2108–2134

Durham WM, Stocker R (2012) Thin phytoplankton layers: characteristics, mechanisms and consequences. Annu Rev Mar Sci 4:177–207

Durham WM, Kessler JO, Stocker R (2009) Disruption of vertical motility by shear triggers formation of thin phytoplankton layers. Science 323:1067–1070

Fiedler PC (1982) Zooplankton avoidance and reduced grazing responses to *Gymnodinium splendens* (Dinophyceae). Limnol Oceanogr 27:961–965

Franks PJS (1992) Sink or swim: accumulation of biomass at fronts. Mar Ecol Prog Ser 82:1–12

Gibson CH, Schwarz WH (1963) The universal equilibrium spectra of turbulent velocity and scalar fields. J Fluid Mech 16:365–384

Gordon HR, Brown OB, Jacobs MM (1975) Computed relationships between the inherent and apparent optical Properties. Appl Opt 14:417–427

Graham GW, Smith WAMN (2010) The application of holography to the analysis of size and settling velocity of suspended cohesive sediments. Limnol Oceanogr Methods 8:1–15

Haury LR, McGowen JA, Wiebe LH 1978. Pattern and processes in the time-space scales of plankton distributions. In: Steele JH (ed) Spatial patterns in plankton communities. Plenum Press, New York NY, p 277–327.

Holliday DV, Pieper RE, Greenlaw CF (1998) Acoustical sensing of small-scale vertical structures. Oceanography 11:18–23

Holliday DV, Donaghay PL, Greenlaw CF, McGehee DE, McManus MM, Sullivan JM, Miksis JL (2003) Advances in defining fine- and micro-scale pattern in marine plankton. Aquat Living Resour 16:131–136

Jeffery GB (1922) The motion of ellipsoidal particles immersed in a viscous fluid. Proc. R. Soc. Lond 102:161–179.

Jericho SK, Garcia-Sucerquia J, Xu W, Jericho MH, Kreuzer HJ (2006) Submersible digital in-line holographic microscope. Rev Sci Instrum 77:043706. doi: 10.1063/1.2193827

Karp-Boss J, Jumars PA (1998) Motion of diatom chains in steady shear flow. Limnol Oceanogr 43:1767–1773

Katz J, Sheng J (2010) Application of holography in fluid mechanics and particle dynamics. Annu Rev Fluid Mech 42:531–555

Katz J, O'Hearn TJ, Acosta AJ (1984) An underwater holographic camera system for detection of micro-particulates. Proc. Cavitation and Multiphase Flow Forum, New Orleans, LA, p 22–25

Katz J, Donaghay PL, Zhang J, King S, Russell K (1999) Submersible holocamera for detection of particle characteristics and motions in the ocean. Deep-Sea Res 46: 1455–1481

Leising AW (2001) Copepod foraging in patchy habitats and thin layers using a 2-D individual-based model. Mar Ecol Prog Ser 216:167–179

Luznik L, Gurka R, Nimmo-Smith WAM, Zhu W, Katz J, Osborn TR (2007) Distribution of energy spectra, Reynolds stresses, turbulence production, and dissipation in a tidally driven bottom boundary layer. J Phys Oceanogr 37:1527–1550

Malkiel E, Alquaddoomi O, Katz J (1999) Measurements of plankton distribution in the ocean using submersible holography. Meas Sci Technol 10:1142–1152

Malkiel E, Abras JN, Katz J (2004) Automated scanning and measurements of particle distributions within a holographic reconstructed volume. Meas Sci Technol 15: 601–612

Marcos, Seymour JR, Luhar M, Durham WM, Mitchell JG, Macke A, Stocker R (2011) Microbial alignment in flow changes ocean light climate. Proc Natl Acad Sci USA 108:3860–3864

McManus MA, Cheriton OM, Drake PJ, Holliday DV, Storlazzi CD, Donaghay PL, Greenlaw CF (2005) Effects of physical processes on structure and transport of thin zooplankton layers in the coastal ocean. Mar Ecol Prog Ser 301:199–215

McManus MA, Kudela RM, Silver MV, Steward GF, Sullivan JM, Donaghay PL (2008) Cryptic blooms: are thin layers the missing connection? Estuar Coast 31:396–401

O'Hern TJ, d'Agostino L, Acosta AJ (1988) Comparison of holographic and Coulter counter measurements of cavitation nuclei in the ocean. J Fluids Eng 110:200–207

Osborn TR (1998) Fine structure, microstructure, and thin layers. Oceanography (Wash DC) 11:36–43

Owen RB, Zozulya AA (2000) In-line digital holographic sensor for monitoring and characterizing marine particulates. Opt Eng 39:2187–2197

Padisák J, Soróczki-Pintér E, Rezner Z (2003) Sinking properties of some phytoplankton shapes and the relation of form resistance to morphological diversity of plankton – an experimental study. Hydrobiologia 500:243–257

Pearson K (1900) On the criterion that a given system of deviations from the probable in the case of a correlated system of variables is such that it can be reasonably supposed to have arisen from random sampling. Philos Mag Series 5 50:157–175

Pfitsch DW, Malkiel E, Ronzhes Y, King S, Sheng J, Katz J

(2005) Development of a free-drifting submersible digital holographic imaging system. OCEANS 2005, Proc MTS/IEEE, Vol 1, p 690–696

Pfitsch DW, Malkiel E, Takagi M, Ronzhes Y, King S, Sheng J, Katz J (2007) Analysis of *in-situ* microscopic organism behavior in data acquired using a free-drifting submersible holographic imaging system. Proc OCEANS 2007, p 1–8 MTS/IEEE

Pope SB (2000) Turbulent flows, 1st edn. Cambridge University Press, Cambridge

Prairie JC, Franks PJS, Jaffe JS (2010) Cryptic peaks: invisible vertical structure in fluorescent particles revealed using a planar laser imaging fluorometer. Limnol Oceanogr 55:1943–1958

Ryan JP, McManus MA, Sullivan JM (2010) Physical, chemical and biological forcing of phytoplankton thin-layer variability in Monterey Bay, California. Cont Shelf Res 30:7–16

Sheng J, Malkiel E, Katz J (2006) Digital holographic microscope for measuring 3D particle distribution and motions. Appl Opt 45:3893–3901

Stacey MT, Margaret MA, Steinbuck JV (2007) Convergences and divergences and thin layer formation and maintenance. Limnol Oceanogr 52:1523–1532

Sullivan JM, Twardowski MS, Donaghay PL, Freeman S (2005) Using optical scattering to discriminate particle types in coastal waters. Appl Opt 44:1667–1680

Sullivan JM, Holliday DV, McFarland M, McManus MA and others (2010a) Layered organization in the coastal ocean: an introduction to planktonic thin layers and the LOCO project. Cont Shelf Res 30:1–6

Sullivan JM, Donaghay PL, Rines JEB (2010b) Coastal thin layer dynamics: consequences to biology and optics. Cont Shelf Res 30:50–65

Sun H, Benzie PW, Burns N, Hendry DC, Watson J (2007) Ocean plankton imaging using an electronic holographic camera. IEEE J Oceanic Eng 32:373–382

Twardowski MS, Sullivan JM, Donaghay PL, Zaneweld J, Ronald V (1999) Micro scale quantification of the absorption by dissolved and particulate material in coastal waters with an ac-9. J Atmos Ocean Technol 16:691–707

Twardowski MS, Boss E, Macdonald JB, Pegau WS, Barnard AH, Zaneveld JRV (2001) A model for estimating bulk refractive index from the optical backscattering ratio and the implications for understanding particle composition in Case I and Case II waters. J Geophys Res 106: 14 129–14 142

Valiela I (1995) Marine ecological processes, 2nd edn. Springer, New York NY

Wang Z, Goodman L (2010) The evolution of a thin layer in strong turbulence. Cont Shelf Res 30:104–118

Watson J, Alexander S, Craig G, Hendry DC and others (2001) Simultaneous in-line and off-axis subsea holographic recording of plankton and other marine particles. Meas Sci Technol 12:L9

Woods JD (1969) On Richardson's number as a criterion for laminar-turbulent-laminar transition in the ocean and atmosphere. Radio Sci 4:1289–1298

Editorial responsibility: Marsh Youngbluth, Fort Pierce, Florida, USA

Submitted: March 23, 2012; Accepted: September 12, 2012
Proofs received from author(s): January 8, 2013